Active Damping of VSG-Based AC Microgrids for Renewable Energy Systems Integration

Yu, Yun

DOI (link to publication from Publisher):
10.54337/aau528211532

Publication date:
2023

Document Version
Publisher's PDF, also known as Version of record

ACTIVE DAMPING OF VSG-BASED AC MICROGRIDS FOR RENEWABLE ENERGY SYSTEMS INTEGRATION

BY
YUN YU

DISSERTATION SUBMITTED 2023

AALBORG UNIVERSITY
DENMARK

ACTIVE DAMPING OF VSG-BASED AC MICROGRIDS FOR RENEWABLE ENERGY SYSTEMS INTEGRATION

Ph.D. Dissertation

Yun Yu

Dissertation submitted month January, 2023

Dissertation submitted: February 2023

PhD supervisor: Prof. Josep M. Guerrero
Aalborg University, Denmark

Assistant PhD supervisor: Assoc. Prof. Sanjay K Chaudhary
Aalborg University, Denmark

PhD committee: Professor Kaiyuan Lu
Aalborg University, Denmark

Professor Ramon Blasco-Gimenez
Technical University of Valencia, Spain

Associate Professor Nursyarizal Mohd Nor
University of Technology Petronas, Malaysia

PhD Series: Faculty of Engineering and Science, Aalborg University

Department: AAU Energy

ISSN (online): 2446-1636
ISBN (online): 978-87-7573-756-7

Published by:
Aalborg University Press
Kroghstræde 3
DK – 9220 Aalborg Ø
Phone: +45 99407140
aauf@forlag.aau.dk
forlag.aau.dk

Printed in Denmark by Stibo Complete, 2023

Curriculum Vitae

Yun Yu

Yun Yu received the B.S. degree in from the China University of Mining and Technology, Xuzhou, China, in 2016, and the M.S. degree from the Tianjin University, Tianjin, China, in 2019, both in electrical engineering. He is currently pursuing the Ph.D. degree at AAU Energy, Aalborg University, Aalborg, Denmark. His research interests include modeling, stability analysis, and control of low-inertia inverter-based systems.

Abstract

For the penetration of renewable-based energy sources, electrical systems in the form of microgrids have been extensively developed, where the interfaces used for interconnecting the prime movers and microgrids are normally based on the power-electronic inverters; however, because of the low-inertia characteristic of power-electronic inverters, AC microgrids may exhibit intensive frequency dynamics. In this manner, the grid-following (GFL) inverter control methods which rely on additional grid-synchronization techniques, may fail to maintain the frequency stability. Then, the grid-forming (GFM) inverter control methods have been considered as solutions to achieve a more reliable integration of renewable-based energy sources. Among these GFM control methods, the virtual synchronous generator (VSG) has gained a lot of attentions. However, its embedded inertia emulation may lead to a poorly damped system with restricted stability margins. This PhD project is conducted to investigate the active-damping methods for VSG-based AC microgrids for a better renewable-energies integration in the future power system. This PhD project was conducted under a joint cooperation with the WindFlag project, a collaborative project between Denmark and Turkey for a large-scale offshore wind power plant integration.

In the literature, active-damping algorithms for VSGs have been continuously investigated, and modifications of the VSG control scheme have been widely reported for either stability boundary extension or low-frequency power oscillation suppression. Nevertheless, these investigations are often conducted without considering the inertial effect, which inevitably leads to the inertial response degradation. Another problem is that the active-damping strategies in most of the existing research works have been proposed on the basis of reduced-order small-signal models. Such models may not provide accurate results, especially when the bandwidth of the current-voltage control is restricted. Moreover, the investigation into the damping-level improvement is mainly conducted using the single-inverter-infinite-bus scenario, whereby the interactions among VSGs in a microgrid are neglected.

To eliminate VSG power oscillations and extend the stability boundary of VSG-based AC microgrids, investigations on the VSG modeling and advance

active-damping strategies have been carried out in this PhD project. Firstly, a power-reference-feedforward control scheme and a fractional order control scheme are proposed. This achieves a smooth active power control without affecting the VSG inertial response. Subsequently, the power-reference-feedforward control scheme is extended for regulating both output active and reactive power. A state-space small-signal model is developed considering the power control, current-voltage control, time delay, virtual impedance and equilibrium point shift. Using this model, a stability-oriented optimal VSG tuning is put forward to extend the stability boundary of VSG-based AC microgrids. Finally, the research is extended to an AC microgrid that includes multiple parallel VSGs. An active-damping strategy which contains self and mutual active damping controllers to eliminate both self-induced and mutually induced power oscillations arising from the parallel operation of VSGs is proposed.

Resumé

Til indtrængen af vedvarende baserede energikilder er der i vid udstrækning udviklet elektriske systemer i form af mikronet, hvor grænseflader, der bruges til at forbinde de primære motorer og mikronet, normalt er baseret på de strømelektroniske invertere; men på grund af den lave inerti-karakteristik af effektelektroniske invertere, kan AC-mikronet udvise intensiv frekvensdynamik. På denne måde kan de net-følgende (GFL) inverterstyringsmetoder, som er afhængige af yderligere netsynkroniseringsteknikker, muligvis ikke opretholde frekvensstabiliteten. Derefter er de grid-forming (GFM) inverterkontrolmetoder blevet betragtet som løsninger til at opnå en mere pålidelig integration af vedvarende-baserede energikilder. Blandt disse GFM-kontrolmetoder har den virtuelle synkrongenerator (VSG) fået en masse opmærksomhed. Dens indlejrede inertieemulering kan dog føre til et dårligt dæmpet system med begrænsede stabilitetsmargener. Dette ph.d.-projekt udføres for at undersøge aktiv-dæmpningsmetoderne for VSG-baserede AC mikronet til en bedre integration af vedvarende energi i fremtidens elsystem. Dette ph.d.-projekt er gennemført i et samarbejde med WindFlag-projektet, et samarbejdsprojekt mellem Danmark og Tyrkiet om en storstilet offshore vindkraftintegration.

I litteraturen er aktiv-dæmpningsalgoritmer for VSG'er løbende blevet undersøgt, og modifikationer af VSG-kontrolskemaet er blevet rapporteret bredt for enten stabilitetsgrænseudvidelse eller lavfrekvent effektoscillationsundertrykkelse. Ikke desto mindre udføres disse undersøgelser ofte uden hensyntagen til inertieffekten, som uundgåeligt fører til inertiresponsforringelsen. Et andet problem er, at de aktive dæmpningsstrategier i de fleste af de eksisterende forskningsarbejder er blevet foreslået på basis af småsignalmodeller af reduceret orden. Sådanne modeller giver muligvis ikke nøjagtige resultater, især når strømspændingsstyringens båndbredde er begrænset. Desuden udføres undersøgelsen af forbedringen af dæmpningsniveauet hovedsageligt ved hjælp af single-inverter-uendelig-bus-scenariet, hvorved interaktionerne mellem VSG'er i et mikronet negligeres.

For at eliminere VSG-effektoscillationer og udvide stabilitetsgrænsen for VSG-baserede AC mikronet, er undersøgelser af VSG-modellering og avancer-

ede aktiv-dæmpningsstrategier blevet udført i dette ph.d.-projekt. For det første foreslås et power-reference-feedforward-kontrolskema og et fraktionelt ordenskontrolskema. Dette opnår en jævn aktiv effektkontrol uden at påvirke VSG-inertiresponsen. Efterfølgende udvides effekt-reference-feedforward-styringsskemaet til regulering af både udgangseffekt og reaktiv effekt. En state-space small-signal model er udviklet under hensyntagen til effektstyring, strømspændingsstyring, tidsforsinkelse, virtuel impedans og ligevægtspunktforskydning. Ved hjælp af denne model fremlægges en stabilitetsorienteret optimal VSG-tuning for at udvide stabilitetsgrænsen for VSG-baserede AC-mikrogids. Endelig udvides forskningen til et AC mikronet, der inkluderer flere parallelle VSG'er. En aktiv dæmpningsstrategi, som indeholder selv- og gensidige aktive dæmpningsregulatorer for at eliminere både selv-inducerede og gensidigt inducerede effektsvingninger, der opstår fra parallel drift af VSG'er, foreslås.

Preface

This Ph.D. thesis summarizes the outcomes from the project "*Active Damping of VSG-based AC Microgrids for Renewable Energy Systems Integration*", which was carried out at AAU Energy, Aalborg University, Denmark.

First of all, I would like to express my sincere gratitude to my supervisor, Prof. Josep M. Guerrero, for providing me with the opportunity to be a part of the CROM. His guidance, encouragement, and constructive suggestions truly helped me during my Ph.D. period. Moreover, I would like to thank my co-supervisors Prof. Juan C. Vasquez and Assoc. Prof. Sanjay K. Chaudhary for their patient guidance and all the kind help.

I would like to thank Prof. José Matas Alcala and Prof. Jorge El Mariachet Carreño for hosting my research stay at Polytechnic University of Catalonia, Spain, and their patient guidance as well as professional suggestions.

My sincere thanks also go to all the colleagues in CROM and friends at AAU for all the kind support and help.

Finally, I would like to express my deepest gratitude to my grandparents, Mr. Honren Li and Mrs. Hondi Hua, my parents, Mr. Yangzhou Yu and Mrs. Shu Li, and my cousins, Mr. Tao Tao, Mrs. Huanhuan Wu, and Han Wu for their endless love and support.

Yun Yu
Aalborg University, February 6, 2023

Contents

Part I

Extended Summary

Chapter 1. Introduction

1 Project Background

1.1 Renewable Energy Growth

After two industrial revolutions in the 18th and 19th centuries, the energy exploitation has moved into a new era where fossil fuels are the major resources to supply the global energy consumption; however, with the industrialization and economic development going on, side effects such as the energy dependency and pollution have become global issues [1]. Then, to meet the increasing energy demand and to fulfill the climate pledge, today's power system is undergoing a rapid transformation towards the low-carbon electricity generation, where renewable energy resources, i.e., hydroelectricity, photovoltaic (PV) and wind, have been continually exploited [2]. Taking wind and solar PV as the examples, as depicted in Fig. 1, significant growths in the installed capacity have been achieved over the years. More specifically, in 2021, the total installed wind power capacity increased to 830 GW, and the total installed solar PV power capacity reached 892 GW [3,4]. Compared with that in 2020, remarkable growths of 12.8% and and 20.4% have been made in the wind and solar PV, respectively.

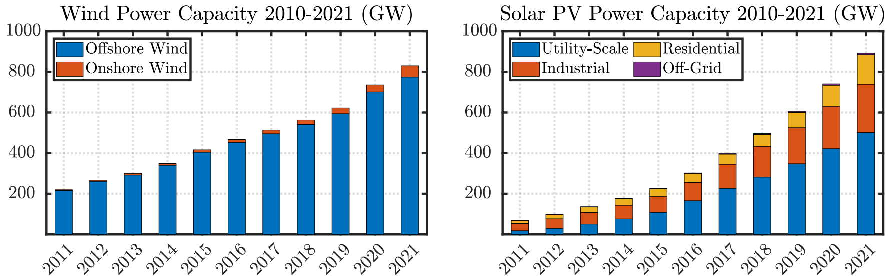

(a) (b)

Fig. 1: Wind and solar PV power capacity 2010-2021. (a) Wind; (b) Solar PV. Source: [3,4].

Even though the growth rate is already among the best that we have ever made, to realize the net-zero carbon dioxide emission, annual capacity additions of wind and solar PV are still expected to accelerate further to bring the share of renewables in the total electricity generation to 88% by 2050 [5]. In this sense, a tremendous amount of inverter-based generators (IBGs) are going to be integrated in the next few decades, taking the form of centralized or distributed renewable energy systems.

1.2 Integration of Renewables in AC Microgrids

As depicted in Fig. 2, today's electric system is still dominated by the conventional power plants, where synchronous machines are dispatched to maintain the system nominal operation, and a certain proportion of IBGs are then integrated following the grid. In the future power systems, IBGs are going to take the role of today's synchronous machines [6]. They can be arranged as utility-scale power plants when there are abandon renewable resources within a remote area. For instance, the Gansu wind farm in desert areas of Gansu province, China is a power plant with a planned power capacity of 20 GW. The Hornsea 1 wind farm, which covers an area of 407 km^3 in the North Sea, is an offshore power plant with the total capacity of 1.2 GW [7]. In general, these utility-scale renewable energy systems are installed far away from the main consumption, and long-distance transmission are then mandatory to make the energy accessible.

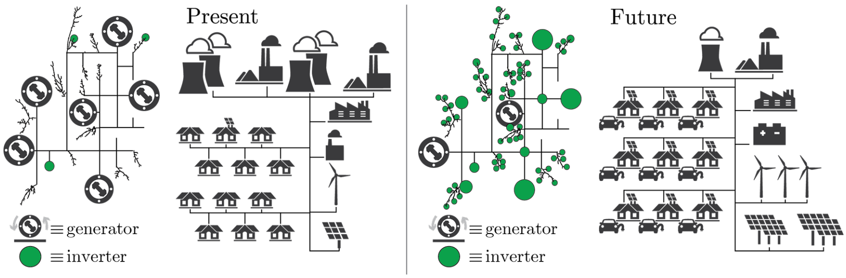

Fig. 2: The present and the future power systems. Source: [6].

In the case that the generation is available at the point of the consumption, the IBGs are normally integrated in the form of microgrids which is interconnected with the utility or run in the islanded mode [8, 9]. For instance, in a project executed by SIEMENS, a campus microgrid with rooftop PV panels, electric vehicle charging stations, and batteries was constructed to meet the local electricity demand [10]. According to the particularity, microgrids are often classified into AC microgrids and DC microgrids, and the former has gained a lot of popularity in practice due to its flexibility in the grid integration [11]. Fig. 3 shows a typical scheme of the AC microgrids, where the generations are composed of conventional generators (e.g., diesel generators) along with the solar PV and wind turbine. Energy storage systems such as battery banks are installed for handling the fluctuating nature of renewables. As the system is AC, the synchronization of different sources is mandatory for the nominal operation. When AC microgrids are integrated into the utility network, voltage and frequency references can be taken from the utility; however, in the islanded operation mode, these references are generated inside AC microgrids using conventional generators or IBGs.

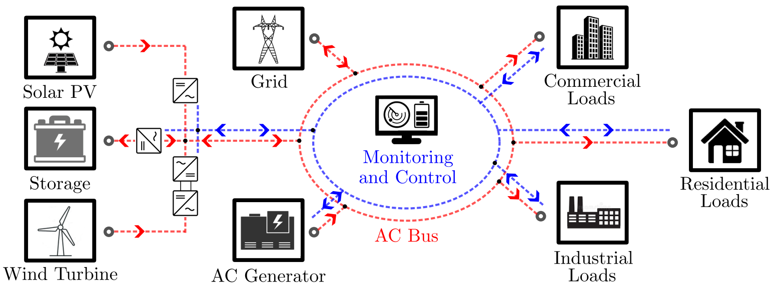

Fig. 3: A typical scheme of AC microgrids.

With respect to the AC microgrids control, the hierarchical architecture has been recognized as a feasible solution to realize intelligent microgrids [8, 12,13]. It has been developed based on the difference in time scales of various microgrid operation set points. In general, the hierarchical architecture can be divided into four levels as following [8,12,13]:

1) Level 0: In this level, basic control loops are often applied to guarantee a stable and fast regulation of the current and voltage.

2) Level 1: This level is normally referred to as the primary control, which takes the responsibility of mimicking the physical behaviors like synchronous machines' droop and inertial characteristics as well as the implementation of output impedance reshaping.

3) Level 2: The correction of microgrid voltage and frequency is integrated in this level to restore the voltage and frequency to the nominal values. Additionally, this level also involves the operation mode switching.

4) Level 3: This is the highest level which is mainly applied for controlling the flow of power among different interconnection points.

It is noteworthy that, considering the microgrid stability, a higher level is normally implemented with a lower control bandwidth. Benefiting from the bandwidth differences, independent modeling and analysis are enabled, where each level can be analyzed assuming others are irrelevant.

1.3 Arising Issues of Integrating Renewables into the Utility

Renewables are mostly connected with utility networks through power electronics that are fundamentally distinct from the traditional synchronous machines. From the perspective of physical characteristics, power electronics exhibit limited inertia and over loading capabilities. From the perspective of control, the renewable energy systems are mostly implemented to follow the grid voltage to extract the maximum power. As a result, side effects like the acceleration of system dynamics, the poor fault ride-through capability, and the frequency and voltage support degradation become critical [14]. According to the stability classification shown in Fig. 4, the arising issues are divided into five groups that correspond to the rotor angle stability, the voltage stability, the frequency stability, the inverter driven stability, and the resonance stability [15,16].

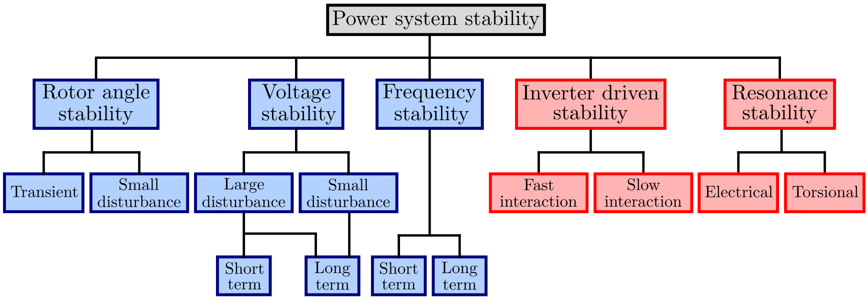

Fig. 4: Power system stability. Source: [15,16].

1) Rotor angle stability: Under severe disturbances, e.g., short-circuit faults on transmission lines, renewable energy systems may degrade the transient stability margins because of the loss of synchronization and the inverter protection [17–19]. Additionally, insufficient damping effects inevitably lead to less stability margins and severe power oscillations under small disturbances [20,21].

2) Voltage stability: Because of the replacement of synchronous machines which take the major responsibility of regulating the grid voltage, the amount of reactive power sources may decrease if renewable energy systems do not provide a reactive power support [22,23]. Consequently, the voltage control capability can be weaken.

3) Frequency stability: One major disadvantage of using inverters as the grid interface is the lack of inertial response. When there is not supplementary control, renewables will not contribute to the system inertia [24,25]. Then, the resulting high rate of change of frequency (RoCoF) may trigger protection and cause cascading disconnections [26].

4) Inverter driven stability: Brought by the interactions among IBGs and the interactions between IBGs and passive components, poorly damped oscillations in a wide frequency range can be driven [27,28].

5) Resonance stability: Caused by series and parallel resonances inside the system, poorly damped oscillations in the purely electrical sense can be introduced [29,30]. When the mechanical system of rotating shafts are involved, torsional vibrations may happen as well [31].

1.4 Grid-Following and Grid-Forming Control

Today, renewable energies are mostly integrated with the grid-following (GFL) control. A typical GFL scheme is depicted in Fig. 5(a), where a phase locked loop (PLL) is adopted for detecting the voltage phase angle at the point of common coupling (PCC) [13]. Then, based on the detected phase angle information, via a fast current regulation, the inverter is directly regulated to inject the required power. Observing from the PCC, as the grid-side current is the physical quantity that is regulated, such a system can be approximately taken as a controlled current source in parallel with a large impedance [13,32], as illustrated in Fig. 5(b). When the inverter run in the islanded mode, since the GFL control needs voltage and frequency references, it cannot work independently. Then, it must shut down.

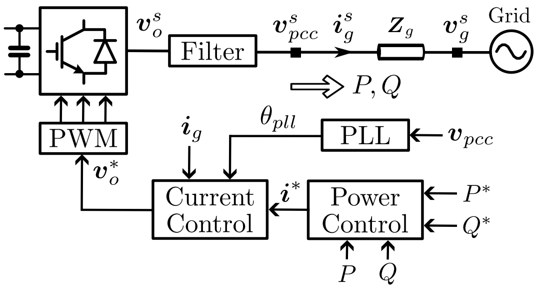

(a)

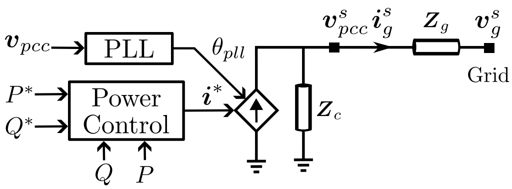

(b)

Fig. 5: GFL inverter. (a) Typical control scheme (b) Simplified representation.

As depicted in Fig. 6(a), the grid-forming (GFM) inverter is mostly implemented without using any dedicated synchronization unit. Instead, through the power control law, the PCC voltage reference is generated, including both phased angle and amplitude information. Using the inner voltage regulation as the basic, the PCC voltage is then regulated to deliver the required power. In this manner, the system can be roughly considered as a voltage source with a small output impedance [13,32], as depicted in Fig. 6(b). Different from the GFL inverter, the GFM inverter can create its own voltage and frequency. Then, even when the system is islanded, it can still work.

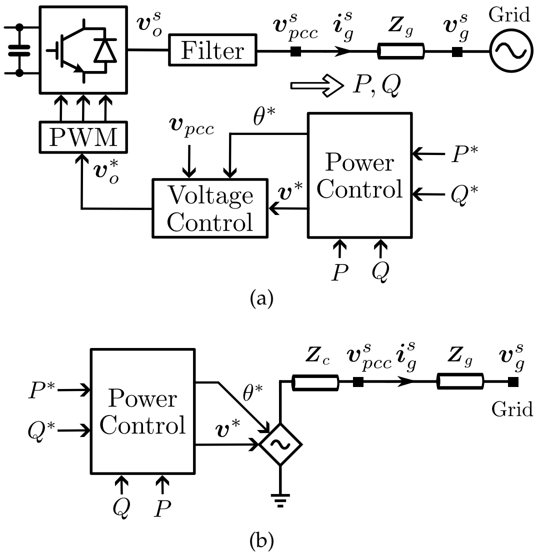

Fig. 6: GFM inverter. (a) Typical control scheme (b) Simplified representation.

A technical feature summary of GFL and GFM controls is presented in Table 1. It is clear that the GFM inverter shares strong similarities with the traditional synchronous machine due to it capability of independently forming the grid. In this sense, it theoretically enables a 100% IBG penetration [33].

Table 1: Technical features of GFL and GFM inverters

GFL Inverter	GFM inverter
PLL is mandatory	PLL is supplementary
Current regulation is the basis	Voltage regulation is the basis
Injecting power is primary	Maintaining grid is primary
Need a grid that is already formed	Form and maintain the grid
Need synchronous machines	Enable a 100% IBG penetration

2 Motivation

In the future power systems, the renewable energy systems are expected to replace the traditional synchronous machines to dominate the electricity generation. In this sense, they are going to take the major responsibility of forming and maintaining a healthy grid; however, facing the arising issues of integrating renewables into the utility network, the GFL control shows restrictions of fulfilling this target due to their dependency on a strong grid. In this sense, the GFM control becomes the key technology for this transformation. Among the existing GFM control concepts for the IBGs, the virtual synchronous generator (VSG) has gained a large popularity in recent years [34].

As a control concept developed on the basis of the synchronous machine emulation, the VSG provides a straight forward synthetic inertia realization that helps slow down the system dynamics. At the same time, because of the inertia emulation, the VSG may exhibit insufficient damping effects, which often results in poorly damped low-frequency power oscillations [35,36]. This may in turn degrade the power quality and increase the risk of interactions with other passive components or voltage sources in the system. Thus, plenty of active damping strategies have been developed to deal with this issue [37]. Nevertheless, these solutions did not consider the damping effect and the inertial effect at the same time. Therefore, the VSG inertial response can be significantly degraded without being noticed.

Apart from this, the analyses of VSGs are often conducted using the phasor representation, where the impacts of inner control loops are disregarded for the analysis simplicity. Such an approximation is accurate only when the inner control loops have enough bandwidths [38]; however, in the case of a limited bandwidth, an appropriate modeling considering current control and voltage control dynamics is essential. Moreover, in practice, the grid impedance may change remarkably, which could significantly affect the control stability and the damping effect; however, the existing VSG tuning algorithms mostly disregard this and only involve one fixed system setting for the offline stability analysis and parameter tuning.

Moreover, in the research works on the active damping of VSGs, investigations are often conducted considering a single unit, whereas the parallel operation of multiple units are not included, especially when they are connected to the external grid. Therefore, under the parallel operation of VSGs, the self-induced oscillations and the interactions among different units cannot be comprehensively considered in the developed active damping strategies. Another issue is that the tuning of these active damping strategies are mostly carried out offline, which means that the same tuning procedure need to be repeated once there are systems setting changes. In practive, such tuning algorithms inevitably increase computational burden.

3 Project Objectives

Considering the aforementioned challenges, this Ph.D. project has been conducted focusing on the development of active damping strategies for VSG-based AC microgrids. The research questions considered in the Ph.D. project are listed as follows:

- How to guarantee the VSG control stability considering that the grid impedance may change remarkably in practice?
- How to alleviate the inertial-effect-induced low-frequency power oscillations in the VSG-based AC microgrid without any degradation of the inertial response?
- How to simultaneously achieve independent and qualitative designs of both VSG power tracking and inertial response?
- How to realize sufficient damping effects for eliminating low-frequency power oscillations that origin from the parallel operation of VSGs in an AC microgrid?

Corresponding to the above questions, the objective of this Ph.D. project is to develop active-damping strategies to eliminate VSG low-frequency power oscillations and to extend the stability boundary of VSG-based AC microgrids. Subobjectives are defined as follows:

- To develop new control schemes to eliminate low-frequency power oscillations while preserving the inertial response of VSG.

  New VSG control schemes, which eliminate inertial-effect-induced low-frequency power oscillations and preserve the inertial response simultaneously, need to be developed. Under the new control schemes, it is expected to achieve independent and quantitative adjustments of both power tracking dynamic and inertial response.

- To develop stability-oriented optimal VSG tuning for extending the stability boundary of VSG-based AC microgrids.

  New VSG tuning algorithms, which consider the grid impedance variation, need to be developed. It is expected that the developed tuning algorithms can be implemented online to optimize the control stability as well as the control dynamics according to the detected grid impedance, automatically.

- To develop new active-damping strategies to eliminate both self-induced and mutually induced low-frequency power oscillations arising from the parallel operation of VSGs.

New active damping strategies, which consider inertial-effect-induced low-frequency power oscillations and interactions among VSGs, need to be developed. It is preferable to enable an automatic tuning of the developed active-damping strategies adapting to the parameter changes in practice, for example, the grid strength, VSG amount, as well as VSG control parameter variations.

4 Thesis Outline

The progress made in the Ph.D. project has been presented in this Ph.D. thesis as a collection of publications. Specifically, the entire thesis can be divided into two parts: *Extended Summary* which includes six chapters and *Selected Publications* which includes manuscripts that are published and still under review processes. For clarity, a graphical outline is shown in Fig. 7

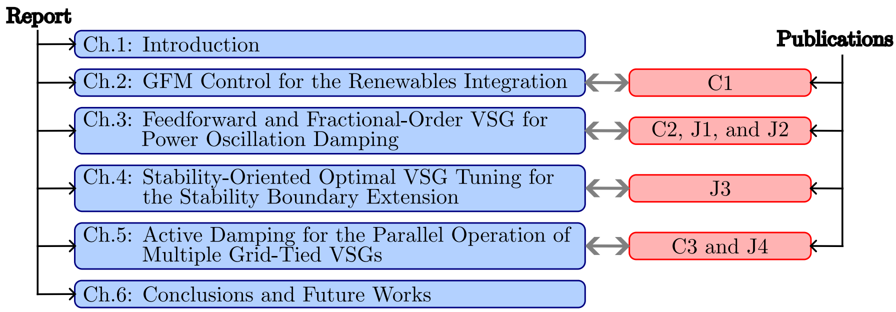

Fig. 7: Graphical outline.

In the first chapter, the research background, the motivation, and the objectives of the Ph.D. project are introduced. Following this, Chapter 2 gives a brief review on the GFM control methods in the existing publications for the renewable energies integration. Corresponds to the first project objective, in Chapter 3, two VSG control schemes which enable the inertia-preserving low-frequency power oscillation attenuation have been introduced. The first scheme adopts the set point feedforward, and the second scheme uses the fractional order control. Afterwords, in Chapter 4, the optimal VSG tuning which reflects the second project objective has been discussed for the extension of stability boundary under grid impedance variations. In chapter 5, the parallel operation of VSG in AC microgrids has been investigated. New active damping strategies for attenuating both self-induced oscillations and the interactions among VSGs have been investigated for the fulfillment of the third project objective. Finally, conclusions derived from this Ph.D. project have been summarized, which leads to a discussion on the project limitations and the future perspectives.

5 List of Publications

Journal Papers

J1 Y. Yu et al., "A Reference-Feedforward-Based Damping Method for Virtual Synchronous Generator Control," in *IEEE Transactions on Power Electronics*, vol. 37, no. 7, pp. 7566-7571, July 2022.

J2 Y. Yu et al., "Fractional Order Virtual Synchronous Generator," submitted to *IEEE Transactions on Power Electronics*, Status: Accepted.

J3 Y. Yu et al., "Multi-Objective Optimal Tuning of Virtual Synchronous Generators With Feedforward Filters," submitted to *Applied Energy*, Status: Under Review.

J4 Y. Yu et al., "Active Damping for Dynamic Improvement of Multiple Grid-Tied Virtual Synchronous Generators," submitted to *IEEE Transactions on Industrial Electronics*, Status: Under Review.

Conference Papers

C1 Y. Yu et al., "An Overview of Grid-Forming Control for Wind Turbine Converters," *IECON 2021 – 47th Annual Conference of the IEEE Industrial Electronics Society*, 2021, pp. 1-6.

C2 Y. Yu et al., "A Comparison of Fixed-Parameter Active-Power-Oscillation Damping Solutions for Virtual Synchronous Generators," *IECON 2021 – 47th Annual Conference of the IEEE Industrial Electronics Society*, 2021, pp. 1-6.

C3 Y. Yu et al., "Accuracy Assessment of Reduced- and Full-Order Virtual Synchronous Generator Models Under Different Grid Strength Cases," *IECON 2022 – 48th Annual Conference of the IEEE Industrial Electronics Society*, 2022, pp. 1-6.

Chapter 2. Grid-Forming Control for the Renewables Integration

1 Introduction

Under a high penetration level of renewables, the conventional GFL integration strategies face obstacles in guaranteeing the safe power system operation. Consequently, a transformation towards the GFM control is undergoing [33]. For this, various GFM control methods have been developed. Based on different concepts, these GFM control methods exhibit distinct properties in the IBGs's synchronization, load sharing, and inertial response, etc. In this chapter, the existing GFM control methods are introduced.

2 An overview of Existing GFM control methods

2.1 Droop Control

Emulating the synchronous machine behavior via droop characteristics, voltage and frequency droop control methods have gained a great popularity for the parallel operation of IBGs in AC and DC microgrids [8]. The well-known formulas that describe the droop principle in AC systems are

$$G_p(s)(P^* - P) = \omega - \omega^*, \; G_q(s)(Q^* - Q) = V - V^* \tag{1}$$

where $G_p(s)$ and $G_q(s)$ are filters for regulating frequency and voltage deviations, respectively. They are normally composed of proportional control coefficients and low-pass filters (LPFs). In practice, DC gains of the filters are essential to keep the IBGs synchronized within the allowed voltage ranges. Regarding the inner controls, current-voltage control and virtual impedance are applied to ensure a stable IBG. A typical control scheme is given in Fig. 8

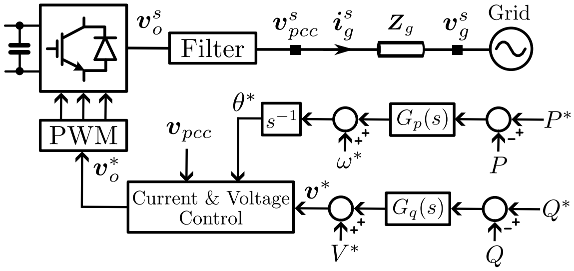

Fig. 8: Typical droop control scheme.

2.2 Virtual Synchronous Generator (VSG)

Being a concept that focuses on improving IBGs' inertia, the VSG was initially developed to smooth the frequency dynamic of inverter-based electric systems under load variations or generation outages [39, 40]. Mimicking the physical inertia of machine's rotational shaft, the swing equation is normally applied for the synchronization and the active power regulation of IBGs as

$$P^* - P = M\frac{d\omega_m}{dt} - D(\omega^* - \omega_m) \tag{2}$$

where ω_m is VSG's angular frequency. M denotes the synthetic inertia, and D denotes the damping constant. With (2) governing the frequency dynamic, the VSG terminal voltage regulation is then designed to mimic the automatic voltage regulator [41]. Following this way, a variety of VSG implementations have been developed in the literature. For instance, the VSG with full-order synchronous machine models [42,43], the VSG with cascaded current-voltage controllers [44], the VSG with additional damping effects from the PLL [35, 45], the VSG with a direct output voltage calculation [46, 47], etc. Despite the differences in the implementation, the core of this concept is still the swing equation (2). Its control scheme is illustrated in Fig. 9

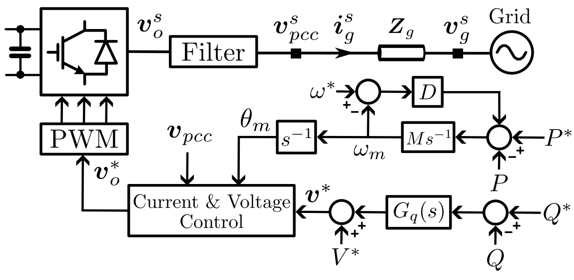

Fig. 9: Typical VSG control scheme.

2.3 Power Synchronization Control (PSC)

This concept was initially developed for attaining a reliable interconnection between the inverter and the ultra-weak grid [48, 49], where the stability of traditional GFL inverters is difficult to be guaranteed because of the negative impacts of PLLs [50]. Its synchronization principle shares strong similarities with the droop control, and it can be formulated as

$$\frac{d\theta^*}{dt} = \omega^* + K_p(P^* - P) \tag{3}$$

where K_p represents the active power control gain. With regard to the voltage amplitude reference, it is generated as

$$\boldsymbol{v}^* = V^* - R_a \frac{s}{s + \omega_b} \boldsymbol{i}_g \tag{4}$$

where Ra is the active resistance, and ω_b denotes the pass band of the high-pass filter (HPF). Applying (3) and (4), the inverter output command is obtained as $\boldsymbol{v}_o^s = \boldsymbol{v}^* e^{j\theta^*}$. A typical PSC scheme is shown in Fig. 10

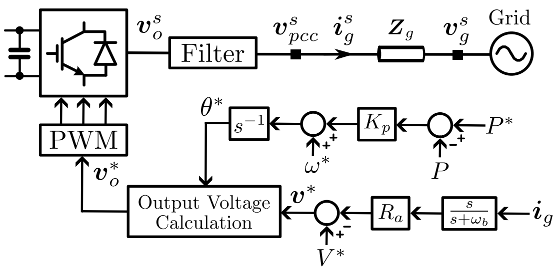

Fig. 10: Typical PSC scheme.

2.4 Virtual Oscillator Control (VOC)

In VOC, explicit regulations of the voltage amplitude and the phase angle are not necessary since the inverter output voltage is directly governed by the digitally-implemented nonlinear oscillators. Then, coupling through the electrical networks, the VOC-based IBGs inherently provide a communicationless synchronization as well as the automatic load sharing [51, 52]. On the other hand, the VOC methods that were initially developed using the Liénard-type oscillators for the islanded systems may not fulfill the set-point tracking requirement in grid-tied applications [53–55]. To tackle the lack of dispatching capabilities, the classical VOC with additional power injection control functions [56] and the hierarchical control frame [57] have been developed.

Moreover, the dispatchable VOC (dVOC) based on the Hopf-type oscillators have been extensively investigated [58,59] as well. In Fig. 11, a typical dVOC scheme is presented.

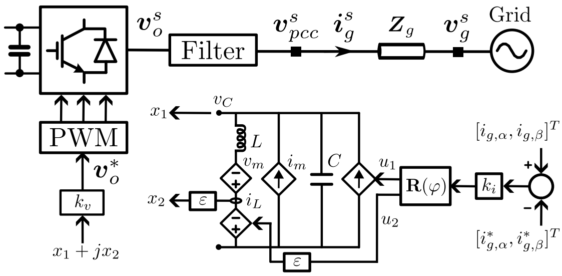

Fig. 11: Typical dVOC scheme.

The resonant LC tank determines the natural resonant frequency $1/\sqrt{LC}$ of the oscillator, and k_v and k_i denote proportional gains for interfacing the oscillator and the inverter. The rotation matrix $\mathbf{R}(\varphi)$ is

$$\mathbf{R}(\varphi) = \begin{bmatrix} \cos\varphi & -\sin\varphi \\ \sin\varphi & \cos\varphi \end{bmatrix} \tag{5}$$

where φ denotes the angle for adjusting the relationship between frequency and voltage amplitude versus active and reactive power. Using x_1 and x_2 (i.e., v_C and εi_L) as two state variables, the controllable voltage v_m and current i_m are formulated as

$$v_m = \xi\sqrt{LC}\left(2X_{nom}^2 - \|x_1 + jx_2\|^2\right)x_2 \tag{6}$$

$$i_m = \frac{\xi\sqrt{LC}}{\varepsilon}\left(2X_{nom}^2 - \|x_1 + jx_2\|^2\right)x_1 \tag{7}$$

where X_{nom} is the RMS value of the oscillation amplitude and ξ denotes the coefficient which controls the convergence rate of the oscillator.

2.5 Matching Control

Different from the numerical synchronous machine emulation, the matching control aims to explore physical links between the synchronous machine and the IBG [60,61]. In matching control, the synchronization is applied using an integral of the DC-link voltage as

$$\frac{d\theta^*}{dt} = \eta V_{dc} \tag{8}$$

where η is a scaling gain. In this manner, the inertia and the damping that correspond to the machine rotor dynamics are linked to the inverter physical quantities. Afterwards, both GFL and GFM control can be implemented by designing different energy functions [61].

3 Summary

In this chapter, the GFM control concepts have been reviewed. It is clear that only the VOC method was proposed by implementing the nonlinear oscillators, and the synchronization of IBGs comes from the inherent properties of the coupled oscillators. Since the VOC algorithm itself is highly nonlinear, the analysis and design inevitably become complex. In addition, its equivalent inertial and droop characteristics are not explicit as the synchronous machines. With respect to the other control methods, namely the droop control, the VSG, the PSC, and the matching control, they were all developed using the synchronous machine emulation. Therefore, they are able to show explicit inertia and droop characteristics. Specifically, the droop control and the PSC mainly provide the droop emulation, and the VSG and the matching control enable both inertia and droop emulations.

Chapter 3. Feedforward and Fractional-Order VSG for the Power Oscillation Damping

1 Introduction

With a straightforward synchronous machine emulation, the VSG has been extensively adopted for different energy conversion applications [41, 62, 63]; however, the favorable synthetic inertia embedded in the VSG may also make the damping effect insufficient, which in turn introduces low-frequency oscillations in the VSG output power [64,65]. To enable a sufficient damping effect on the low-frequency power oscillations, active damping strategies based on different concepts have been continuously investigated [35, 36, 45, 66–68].

In the literature, additional damping effects for attenuating the VSG output power oscillation were realized by using the frequency slip that is detected from the PLL [35, 45]. Although the damping effect can be enhanced by these strategies will PLLs, the PLL-related stability issues are the obstacles in practice [69]. Without using PLLs, Dong et al. proposed the damping correction control method in [66], where the modification of the damping effect was achieved by filtering the power feedback. Similarly, in [67], angular frequency feedback filters were adopted by Shuai et al. for the active damping. Although the damping effect can be improved to some extent by these strategies, the degrees of freedom is limited to adjust the power control dynamic as desired. To achieve more flexibility, an active damping strategy adopting the full state feedback was developed by Liu et al. in [36]. In addition, enabling a fully adjustable power control dynamic, an active damping strategy using the angular acceleration was proposed by Chen et al. in [68]. One common issue of these active damping strategies is that the investigations were conducted mainly on the set-point tracking dynamic, whereas the VSG inertial response was disregarded, as it was pointed out in [70].

2 Modeling of the VSG Based on the Phasor Representation

Fig. 12 depicts the schematic of the VSG that is connected to the grid, where v_{dc} denotes the DC-link voltage. Without loss of generality, the DC-link is taken as ideal source that is well regulated by other components. Thus, its dynamic is not considered in the modeling and the analysis. Moreover, R_f and L_f represent converter-side resistance and inductance, and C_f denotes the capacitance of the LC filter. The grid-side impedance is denoted by $\boldsymbol{Z}_g$. In this chapter, the boldface letters are adopted for the complex vectors, and the superscript s denotes the complex vectors in the $\alpha\beta$ frame, for example, $\boldsymbol{v}_o^s$, $\boldsymbol{i}_f^s$, $\boldsymbol{v}_f^s$, $\boldsymbol{i}_g^s$, and $\boldsymbol{v}_g^s$. The vectors in the VSG's dq frame are formulated without the superscript s, for example, $\boldsymbol{v}_o^*$, $\boldsymbol{i}_f^*$, $\boldsymbol{i}_f$, $\boldsymbol{v}_f$, $\boldsymbol{i}_g$.

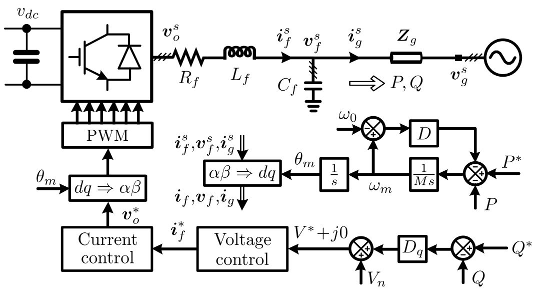

Fig. 12: Schematic of the grid-tied VSG.

Firstly, it is to be expected that the inner current-voltage control is much faster than the VSG's power control, which is a normal case for the applications at a low voltage. Subsequently, the capacitor voltage can be approximately taken as a voltage phasor $V^*\angle\theta_m$ whose amplitude and phase angle correspond to the VSG's power control [71]. Adopting the same expression, the grid voltage is written as $V_g\angle\theta_g$. Then, the angel difference δ between θ_m and θ_g can be formulated as follows:

$$\delta = \theta_m - \theta_g \triangleq \int \left(\omega_m - \omega_g\right) dt \tag{9}$$

where ω_m and ω_g denote the VSG's and grid angular frequency, respectively.

The grid impedance $\boldsymbol{Z}_g$ is considered as mainly inductive, which leads to $\boldsymbol{Z}_g \approx X_g$. In the case that the grid resistance is not small enough that its effect can be disregarded, the virtual impedance is then applied for reshaping the equivalent impedance [72]. In this manner, we have [73]

$$P = \frac{3V^* V_g \sin\delta}{2X_g}, \; Q = \frac{3V^*\left[V^* - V_g\cos(\delta)\right]}{2X_g}. \tag{10}$$

Under normal operation conditions, the grid voltage amplitude V_g almost remains the same. In this manner, it can be considered as a physical quantity without any perturbation. The amplitude of the VSG's voltage and that of the external grid, i.e., V^* and V_g, can be roughly set to the nominal voltage amplitude V_n, i.e., $V^* \approx V_g \approx V_n$. The angle difference δ in (9) is often within the range that the approximations $\sin\delta \approx \delta$ and $\cos\delta \approx 1$ can be applied. Then, applying these approximations, from (10), the the VSG's power perturbations are formulated as follows:

$$\Delta P = \frac{\partial P}{\partial \delta}\Delta\delta + \frac{\partial P}{\partial V_t}\Delta V_t = \frac{3V_n^2}{2X_g}\Delta\delta + \frac{3V_n\delta_n}{2X_g}\Delta V_t, \tag{11}$$

$$\Delta Q = \frac{\partial Q}{\partial \delta}\Delta\delta + \frac{\partial Q}{\partial V_t}\Delta V_t = \frac{3V_n}{2X_g}\Delta V_t + \frac{3V_n^2\delta_n}{2X_g}\Delta\delta \tag{12}$$

where δ_n is the angle difference that corresponds to the equilibrium point.

Taking $G_p(s)$ and $G_q(s)$ as the VSG's power controllers, the power control laws are formulated in the s-domain as follows:

$$\theta_m = \frac{G_p(s)}{s}\left(P^* - P\right),\ V^* = G_q(s)\left(Q^* - Q\right). \tag{13}$$

From (9), (11), (12), and (13), the close-loop systems in the sense of small signal, namely $\Delta P/\Delta P^*$ and $\Delta Q/\Delta Q^*$, are formulated as

$$\frac{\Delta P}{\Delta P^*} = \frac{\frac{3V_n^2G_p(s)}{2X_gs}\left[1 - \frac{3V_nG_q(s)}{2X_g+3V_nG_q(s)}\delta_n^2\right]}{1 + \frac{3V_n^2G_p(s)}{2X_gs}\left[1 - \frac{3V_nG_q(s)}{2X_g+3V_nG_q(s)}\delta_n^2\right]}, \tag{14}$$

$$\frac{\Delta Q}{\Delta Q^*} = \frac{\frac{3V_nG_q(s)}{2X_g}\left[1 - \frac{3V_n^2G_p(s)}{2X_g+3V_n^2G_p(s)}\delta_n^2\right]}{1 + \frac{3V_nG_q(s)}{2X_g}\left[1 - \frac{3V_n^2G_p(s)}{2X_g+3V_n^2G_p(s)}\delta_n^2\right]} \tag{15}$$

3 Development of the Feedforward VSG Control Scheme

As shown in Fig. 12, the conventional VSG's angular frequency is generated by the active power control as

$$P^* - P = M\frac{d\omega_m}{dt} - D(\omega_0 - \omega_m) \tag{16}$$

where ω_m and ω_0 denote VSG and nominal grid frequency. M and D denote the synthetic inertia and the damping constant. M is equal to $2HS_{base}/\omega_0$, where H denotes the inertia constant, and S_{base} denotes the VSG rated power. From (16), the active power controller $G_p(s)$ can be derived as $(Ms + D)^{-1}$.

Substituting $G_p(s)$into (14), and setting $\delta_n = 0$ to disregard the coupling effect, the close-loop system $\Delta P/\Delta P^*$ is written as

$$\frac{\Delta P}{\Delta P^*} = \frac{3V_n^2}{2MX_g s^2 + 2DX_g s + 3V_n^2}. \tag{17}$$

From (17), it can be seen that $\Delta P/\Delta P^*$ becomes a second-order plant. In practice, V_n and X_g are not adjustable, and D is often fixed for a predefined static droop emulation. Then, once the synthetic inertia M is not set appropriately, complex eigenvalues with insufficient damping effects are introduced, and the power control dynamic will get oscillatory. To handle the resulting power oscillations, the reference-feedforward (RFF) controller $G_{RF}(s)$ is proposed, and the VSG control scheme is modified as Fig. 13.

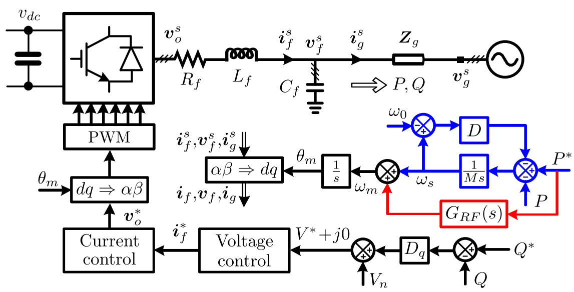

Fig. 13: Schematic of the grid-tied VSG applying the RFF controller.

From Fig. 13, it can be observed that, with the RFF controller $G_{RF}(s)$, the VSG active power control law becomes [74]

$$P^* - P = M\frac{d\omega_s}{dt} + D\left(\omega_s - \omega_0\right), \tag{18}$$

$$\omega_m = P^* G_{RF}(s) + \omega_s \tag{19}$$

where ω_s denotes the angular frequency without the feedforward compensation. From (19), it is clear that the VSG angular frequency ω_m is a combination of the ω_s and the RFF term $P^* G_{RF}(s)$. To avoid affecting the static droop emulation, the RFF controller $G_{RF}(s)$ should be able to filter out the DC contents in the power set point. For this, the $G_{RF}(s)$ can be selected as

$$G_{RF1}(s) = k_{hp1}\frac{s}{s + k_{hp2}} \tag{20}$$

where k_{hp1} and k_{hp2} are two coefficients used to adjust the frequency response of $G_{RF1}(s)$. Combining (14), (18), (19), and (20), setting $\delta_n = 0$ to disregard the coupling effect, the close-loop system $\Delta P/\Delta P^*$ is then reconstructed as

$$\frac{\Delta P}{\Delta P^*} = \frac{3V_n^2\left[Mk_{hp1}s^2 + \left(Dk_{hp1} + 1\right)s + k_{hp2}\right]}{\left(2MX_g s^2 + 2DX_g s + 3V_n^2\right)\left(s + k_{hp2}\right)}. \tag{21}$$

Here, it is clear that an extra real eigenvalue is $-k_{hp2}$, and there are two additional zeros which are determined by k_{hp1} and k_{hp2}. For a smooth power control dynamic with less oscillations, it is preferable to place these two extra zeros close to the original poorly damped complex eigenvalues. In this manner, the power control dynamic can be roughly dominated by the newly introduced real eigenvalue. Considering this, a sweep of the coefficients k_{hp1} and k_{hp2} is applied, as shown in Fig. 14.

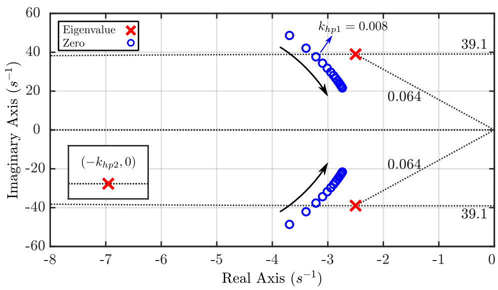

Fig. 14: Pole-zero map of $\Delta P/\Delta P^*$, where k_{hp1} changes from 0.006 to 0.03, $k_{hp2} = 1000$, $H = 5$ s, $D = 50$ pu, $V_n = 380\sqrt{2/3}$ V, $S_{base} = 2.2$ kVA, $\omega = 100\pi$ rad/s, and $X_g = 1.35\ \Omega$. [74]

From (21), it is clear that the RFF controller $G_{RF1}(s)$ can only alleviate the power oscillations, whereas a complete mitigation cannot be attained. The root reason is that the degrees of freedom is not enough. Considering this, another way of deriving the RFF controller is presented. Assuming that the close-loop system $\Delta P/\Delta P^*$ becomes a typical second-order system as [74]

$$\frac{\Delta P}{\Delta P^*} = \frac{\omega_n^2}{s^2 + 2\zeta\omega_n s + \omega_n^2} \tag{22}$$

where ω_n represents the natural frequency, and ζ is the damping ratio. They correspond to the desired power control dynamic. Subsequently, combining (14), (18), and (19), setting $\delta_n = 0$ to disregard the coupling effect, the RFF controller $G_{RF2}(s)$ can be derived as

$$G_{RF2}(s) = \frac{m_2 s^2 + m_1 s}{3V_n^2\left(Ms^3 + n_2 s^2 + n_1 s + D\omega_n^2\right)} \tag{23}$$

where the coefficients m_1, m_2, n_1, and n_1 are

$$\begin{aligned} m_2 &= 2M\omega_n^2 X_g - 3V_n^2, \quad m_1 = 2D\omega_n^2 X_g - 6V_n^2\zeta\omega_n, \\ n_2 &= D + 2M\zeta\omega_n, \quad n_1 = M\omega_n^2 + 2D\zeta\omega_n. \end{aligned} \tag{24}$$

Here, it can be seen that the coefficients of the RFF controller $G_{RF2}(s)$ are written using the VSG settings M and D, the natural frequency ω_n, and the damping ratio ζ. Therefore, in practice, $G_{RF2}(s)$ is able to be automatically tuned online for the desired power control dynamic, provided that the grid side inductance X_g is known. In terms of the selection of ω_n and ζ, following the classical control theory, the damping ratio ζ is firstly selected around 0.9. Then, the natural frequency ω_n is directly calculated as $\omega_n = 0.25\zeta T_{set}$ [74]. T_{set} corresponds to the desired settling time of the VSG's power control.

In the above analyses, the RFF controllers $G_{RF1}(s)$ and $G_{RF2}(s)$ are tuned without considering the coupling effect as $\delta_n = 0$ is applied to remove the coupling terms in (14). To assess the influence of the coupling effects, combining (14), (18), and (19), assuming that δ_n is not zero, the close-loop system $\Delta P/\Delta P^*$ with the RFF controller and the coupling effects is derived as

$$\frac{\Delta P}{\Delta P^*} = \frac{\left[\frac{3V_n^2}{2X_g s(Ms+D)} + \frac{3V_n^2}{2X_g s} G_{RF}(s)\right]\left[1 - \frac{3V_n D_q}{2X_g + 3V_n D_q}\delta_n^2\right]}{1 + \frac{3V_n^2}{2X_g s(Ms+D)}\left[1 - \frac{3V_n D_q}{2X_g + 3V_n D_q}\delta_n^2\right]}. \tag{25}$$

Substituting (20) and (23) into (25), setting δ_n to 1 for the excessive coupling effects, varying the reactive power control coefficient D_q from 0 pu to 10 pu, the eigenvalue placement is shown in Fig. 15. it is clear that, the coupling effects have no obvious impact on the desired eigenvalue placement.

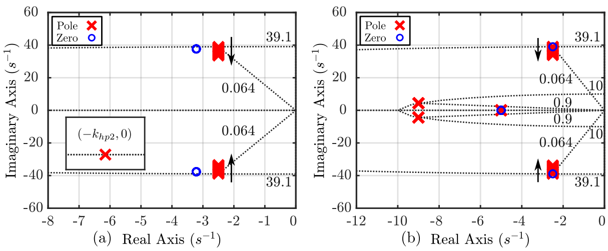

Fig. 15: Pole-zero map of $\Delta P/\Delta P^*$, where D_q is within [0 10] pu, $H = 5$ s, $D = 50$ pu, $V_n = 380\sqrt{2/3}$ V, $S_{base} = 2.2$ kVA, $\omega = 100\pi$ rad/s, and $X_g = 1.35\ \Omega$. (a) $G_{RF1}(s)$ is adopted (k_{hp1} is 0.008 and k_{hp2} is 1000); (b) $G_{RF2}(s)$ is adopted (ζ is 0.9 and ω_n is 10 rad/s). [74]

4 Development of the Fractional-Order VSG Control Scheme

As it was discussed in the previous section, causing by the lack of degrees of freedom, the conventional VSG often exhibits an oscillatory power control. Then, to alleviate the power oscillations, the synthetic inertia is tuned for less inertial effects. Although the inertial-effect-induced power oscillations will be eased to some extent, the preferable inertial response will be inevitably degraded as well. A compromise between the power set point tracking and the inertial response becomes a necessity. Considering this issue, the fractional-order control (FOC) is applied to introduce more degrees of freedom.

In FOC, the operator order can be non-integer, whereas the basic properties of the integration and the differentiation can be preserved [75]. Applying the FOC, the VSG active power control law is modified as

$$P^* - P = M\frac{d^{\gamma+\lambda}\omega_f}{dt} + D_1\frac{d^{\gamma}\omega_f}{dt} + D_2\omega_f, \tag{26}$$

$$\omega_m = \omega_0 + \omega_f. \tag{27}$$

The corresponding control scheme is depicted in Fig. 16.

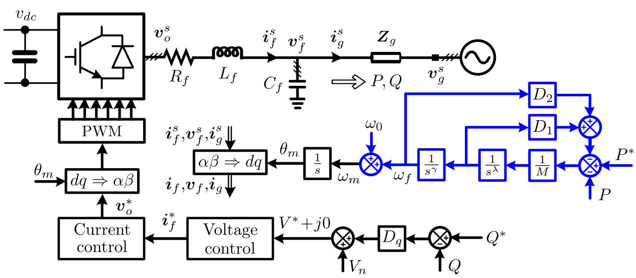

Fig. 16: Schematic of the grid-tied fractional-order VSG.

Combining (26), (27), and (14), disregarding the coupling effect, the loop gain $G_l(s)$ of the close-loop system $\Delta P/\Delta P^*$ is formulated as

$$G_l(s) = \frac{1}{Ms^{\gamma+\lambda} + D_1 s^{\gamma} + D_2}\frac{3V_n^2}{2X_g s}. \tag{28}$$

Following the derivation in [64] and [76], the VSG inertial effect is evaluated by $\Delta\omega_m/\Delta P$ as

$$F(s) = \frac{1}{Ms^{\gamma+\lambda} + D_1 s^{\gamma} + D_2}. \tag{29}$$

To implement and tune the proposed fractional-order VSG for the desired power control dynamic and the enhanced inertial response, the oustaloup recursive approximation is applied as [77]

$$s^o = K\prod_{k=1}^{N}\frac{s+\omega_k'}{s+\omega_k} \tag{30}$$

where o denotes the operator order which is a fractional number. N is the oustaloup filter order. K, ω_k', and ω_k are filter coefficients that are written as

$$K = \omega_h^o,\ \omega_k' = \omega_l\omega_u^{\frac{2k-1-o}{N}},\ \omega_k = \omega_l\omega_u^{\frac{2k-1+o}{N}},\ \omega_u = \sqrt{\omega_h/\omega_l} \tag{31}$$

where ω_l and ω_h are the minimum and the maximum frequencies that of interest. In general, N is 5, and ω_l and ω_h are set to 0.1 and 1000 rad/s [75].

Here, for the fractional-order VSG tuning, preconditions are defined as

i) The sum of the order of two fractional operators is equal to 1: $\gamma + \lambda = 1$ where $\gamma \in (0, 1)$ and $\lambda \in (0, 1)$.

ii) The original static droop emulation is not affected: $\lim_{s \to 0} F(x) = -D^{-1}$.

It is clear that, following these preconditions, the original four coefficients, i.e., γ, λ, D_1, and D_2 can be reduced by half, which significantly simplifies the tuning process. Then, considering the control stability and the control dynamic, three criteria have been defined as follows:

a) To make the fractional-order VSG truly stable, it is mandatory to make both D_1 and D_2 always positive: $D_1 > 0$ and $D_2 > 0$.

b) The phase margin φ_M and the crossover frequency ω_{cg} that are derived from the loop gain (28) are used as the main measures of the close-loop system $\Delta P / \Delta P^*$. Their thresholds are set to 30° and 18 rad/s for both acceptable stability margins and control dynamics [78].

c) The cutoff frequency ω_c that is derived from (29) serves as the index of the inertial response. The inertial effect tends to be stronger when the value of ω_c is smaller.

Then, the phase margin φ_M, the crossover frequency ω_{cg}, as well as the cutoff frequency ω_c are plotted on the γ-D_1 plane as Fig. 17.

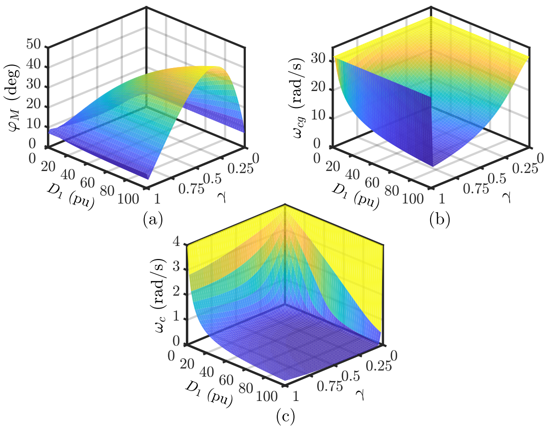

Fig. 17: Main measures for the fractional-order VSG tuning, where $\gamma \in (0, 1)$, $D_1 \in (0, 100)$ pu, $H = 2.5$ s, $D = 20$ pu,$V_n = 220\sqrt{2/3}$ V, $S_{base} = 2.2$ kVA, $\omega = 100\pi$ rad/s, and $X_g = 1.8\ \Omega$ (a) The phase margin φ_M; (b) The crossover frequency ω_{cg}; (c) The cutoff frequency ω_c.

As shown in Fig. 17(c), applying the fractional-order VSG control scheme, the cutoff frequency ω_c reduces remarkably on the entire γ-D_1 plane. Thus, the inertial response is always better than that of the conventional VSG.

As the inertial response enhancement is fulfilled, the predefined criteria a) and b) are used to generate the feasible parameter range. As depicted in Fig. 18, the gray region corresponds to the feasible parameter range for γ and D_1. Once γ and D_1 are selected within the feasible range, λ and D_2 can be directly calculated according to the preconditions i) and ii).

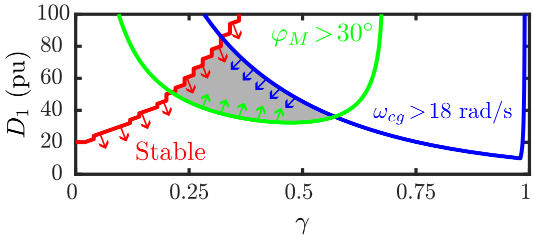

Fig. 18: The feasible parameter range for γ and D_1, where $H = 2.5$ s, $D = 20$ pu, $V_n = 220\sqrt{2/3}$ V, $S_{base} = 2.2$ kVA, $\omega = 100\pi$ rad/s, and $X_g = 1.8\ \Omega$.

5 Simulation and Experimental Validations

For validating the feasibility of the proposed VSG control schemes, EMT simulations in Digsilent and analyses in Matlab are applied. The experimental implementation shown in Fig. 19 is adopted for the validation as well. Two kinds of scenario are considered in the validations: i) a grid-tied VSG with power set point change is applied to check the power control ii) an islanded VSG with load change is used for validating the inertial response.

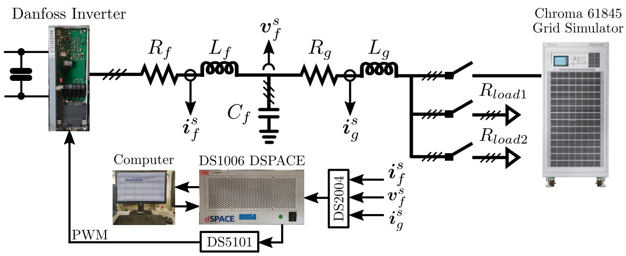

Fig. 19: The experimental implementation.

5.1 Validations of the Feedforward VSG Control Scheme

Settings used for the validations are presented in Table 2. The corresponding simulation validations in Digsilent are presented in Fig. 20. It can be observed that, under a set point step change, the VSG without the RFF controller shows

Table 2: Settings for the feedforward VSG control scheme validation

Variable	Values	Variable	Values
S_{base}	2.2 kVA	ω_0	100π rad/s
V_n	$380\sqrt{2/3}$ V	V_{dc}	650 V
L_f	3.6 mH	R_f	0.1 Ω
C_f	9 μF	L_g	4.3 mH
R_g	0.5 Ω	f_{sw}	10 kHz
H	5 s	D	50 pu
D_q	0.1 pu		
k_{hp1}	0.03	k_{hp2}	1000
ζ	0.9	ω_n	10 rad/s

an oscillatory output, and the oscillation frequency is around 6 Hz. When the proposed RFF controller $G_{RF1}(s)$ is applied, the low-frequency power oscillations are alleviated remarkably. The power control dynamic is dominated by the real eigenvalue as it was analyzed before. When the proposed RFF controller $G_{RF2}(s)$ is applied, the power control is well damped. No low-frequency power oscillations can be found, and the settling time is as expected. With regard to the inertial response, as shown in Fig. 20 (b), not only the frequency profile is similar, but the RoCoF values are also the same. It indicates that the VSG's inertia is preserved without any degradation.

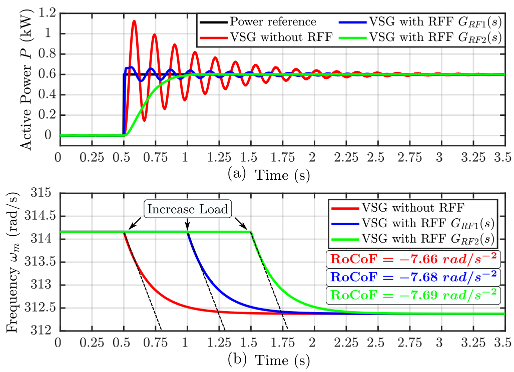

Fig. 20: Simulation validation of the VSG with and without the RFF controllers. (a) Output active power P of the grid-tied VSG; (b) Angular frequency ω_m of the islanded VSG. [74]

The experiment validations are shown in Fig. 21 and 22. From the experimental validations, the same conclusions can be derived that the proposed feedforward control scheme can effectively alleviate the poorly-damped oscillations in the VSG's output with the same inertial response.

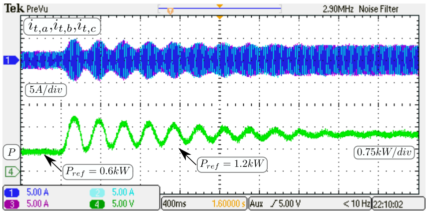

(a)

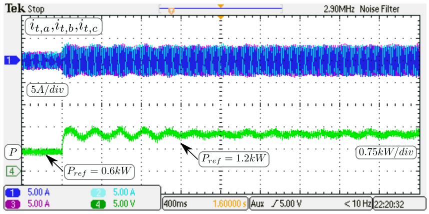

(b)

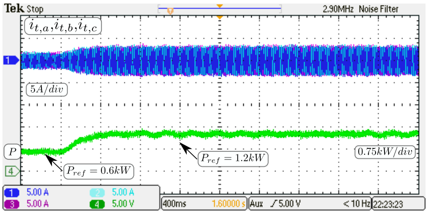

(c)

Fig. 21: Experimental validation in the grid-tied mode. (a) Without the proposed RFF controllers; (b) With $G_{RF1}(s)$; (c) With $G_{RF2}(s)$. [74]

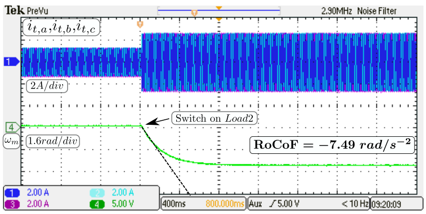

(a)

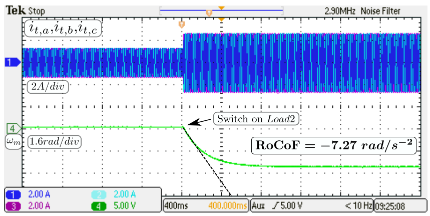

(b)

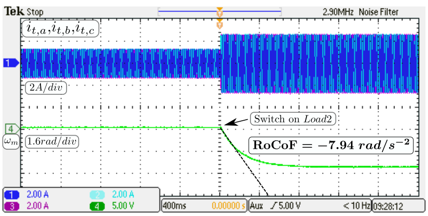

(c)

Fig. 22: Experimental validation in the islanded mode. (a) Without the proposed RFF controllers; (b) With $G_{RF1}(s)$; (c) With $G_{RF2}(s)$. [74]

5.2 Validations of the Fractional-Order VSG Control Scheme

In this subsection, the validations of the proposed fractional-order VSG control scheme are presented, the used system settings are presented in Table 3.

Table 3: Settings for the fractional-order VSG control scheme validation

Variable	Values	Variable	Values
S_{base}	2.2 kVA	ω_0	100π rad/s
V_n	$220\sqrt{2/3}$ V	V_{dc}	650 V
L_f	1.8 mH	R_f	0.1 Ω
C_f	9 μF	L_g	5.5 mH
R_g	0.5 Ω	f_{sw}	10 kHz
H	2.5 s	D	20 pu
γ	0.43	λ	0.57
D_1	52 pu	D_2	12.8 pu

Using the presented system settings, the analytical comparisons are firstly applied. As depicted in Fig. 23, using the proposed fractional-order VSG, the power oscillations under the set point step change are well attenuated, which indicates that stronger damping effects are introduced. The inertial response has been significantly improved at the same time as it can be seen in both the RoCoF during the transient and the angular frequency settling time.

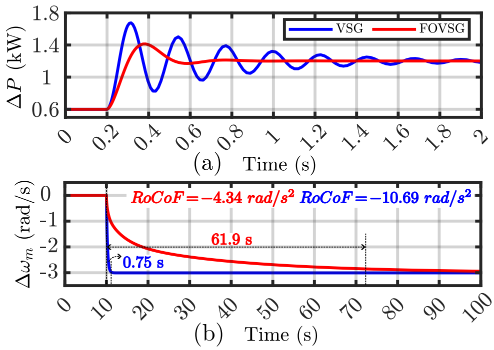

Fig. 23: Analytical comparisons of the conventional VSG and the fractional-order VSG. (a) Output active power perturbation ΔP of the grid-tied VSG; (b) Angular frequency perturbation $\Delta\omega_m$ of the islanded VSG.

Corresponding experimental validations are presented in Fig. 24 and 25. Here, similar to the analytical results, under the set point step change, sustained oscillations are in the conventional VSG's output. On the other hand, under the same operation condition, the fractional-order VSG shows a well-damped power control dynamic. With respect to the inertial response, it is clear that the angular frequency settling time is remarkably extended by the fractional-order VSG (from 0.84 s to 58.7 s), as shown in Fig.25(a) and 25(b). Moreover, the RoCoF reduces from -9.87 rad/s^2 to -4.03 rad/s^2, as shown in Fig. 25(c) and 25(d).

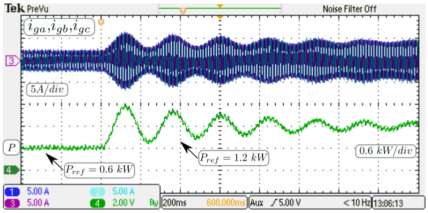

(a)

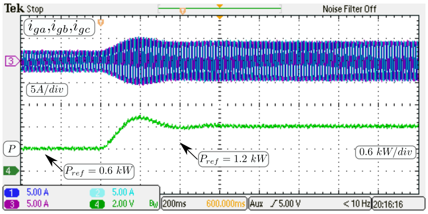

(b)

Fig. 24: Experimental validation of the grid-tied VSG. (a) VSG; (b) Fractional-order VSG.

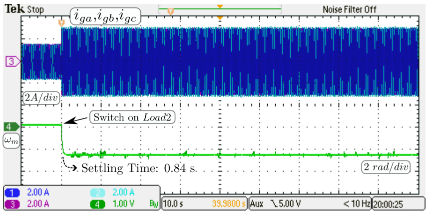

(a)

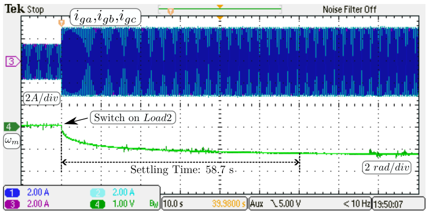

(b)

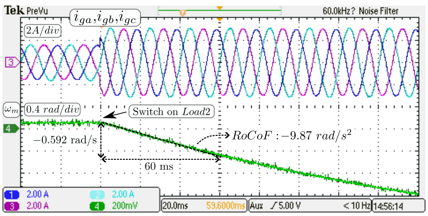

(c)

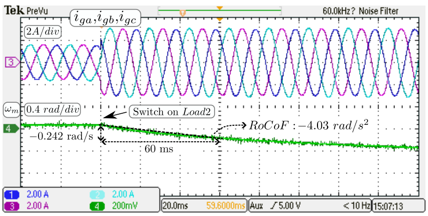

(d)

Fig. 25: Experimental validation of the islanded VSG. (a) VSG; (b) Fractional-order VSG; (a) Zoom of the VSG; (b) Zoom of the fractional-order VSG.

6 Summary

In this chapter, the VSG's small-signal model is derived based on its phasor representation. Following this, a novel feedforward VSG is developed to alleviate the inertial-effect-induced power oscillations and preserve the inertial response, simultaneously. The proposed feedforward VSG control scheme features in enabling an independent and quantitative design of the power tracking dynamic and the VSG inertial response. Furthermore, to provide a preferable power tracking without any low-frequency power oscillation and an enhanced VSG inertial response simultaneously, the fractional-order VSG control scheme is proposed. Then, through the analytical, simulation , and experimental validations, the feasibility of these two novel control schemes has been validated.

Chapter 4. Stability-Oriented Optimal VSG Tuning for the Stability Boundary Extension

1 Introduction

The VSG control stability is normally analyzed using the phasor representation, where the VSG-regulated IBG is approximately taken as a controllable voltage source for simplicity. For instance, the VSG large-signal stability under the grid voltage dips have been analyzed in [79] and [80] using the phasor representation. Also, applying the same phasor representation, the VSG small-signal stability analyses can be found in [64, 65, 76, 81]. Although the analysis accuracy based on the phasor representation can be ensured in the most of the cases, the mismatches will inevitably get non-negligible when the inner current-voltage control is restricted by the control latency.

For a better accuracy, the VSG stability analysis adopting high-order models has been extensively investigated. For example, a trial-and-error VSG tuning approach based on a 8th-order model was developed in [82] for the VSG control stability. Moreover, a further improvement with the quantitative criteria was made in [83] to alleviate the VSG tuning effort. Additional investigations that use the detailed VSG model to identify the instability were conducted in [38, 84, 85]. In these studies, the system settings are assumed to be fixed, which is not practical in real applications since the analysis needs to be repeated once there are system setting changes. Considering this, the iteration tuning algorithm in [44] was developed to enable an automatic online VSG tuning; however, it may exhibit a slow convergence speed. Another issue of the VSG operation is the insufficient damping effect and its resulting low-frequency power oscillations which are often disregarded in the these studies; In this sense, to simultaneously realize the extended VSG stability boundary and optimal power control dynamic is of practical significance.

2 Modeling of the VSG Based on the State-Space Representation

2.1 System Description

Fig. 26 shows a grid-tied VSG to be investigated in this chapter. It contains the inner current-voltage regulation, virtual impedance, and two power control loops. Same as the denotation used in Chapter 3, here, the boldface letters denote the complex vectors, and the superscript s is utilized to distinguish vectors on the $\alpha\beta$ and dq frames.

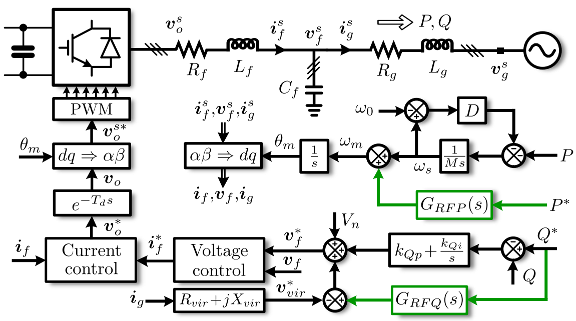

Fig. 26: Schematic of the grid-tied VSG with feedforward controllers.

Firstly, the VSG active power control is reconstructed as

$$\omega_m = \omega_s + G_{RFP}(s)P^*, \ -P = M\frac{d\omega_s}{dt} + D\left(\omega_s - \omega_0\right) \tag{32}$$

where ω_m and ω_0 represents the VSG's and the nominal grid frequency. ω_s denotes the angular frequency generated from the power feedback. M and D represent the synthetic inertia and the damping constant. M is equal to $2HS_{base}/\omega_0$, where H denotes the inertia constant, and S_{base} is the inverter capacity. $G_{RFP}(s)$ denotes the feedforward controller for the VSG active power control, and it is obtained following the same derivation used in Chapter 3. Specifically, it is firstly assumed that the coupling effect in (14) is negligible, and it becomes a first-order plant as $1/(T_P s + 1)$ when the feedforward controller $G_{RFP}(s)$ is applied. Then, from (14) and (32), $G_{RFP}(s)$ is derived as

$$G_{RFP} = \frac{Ms^2 + Ds + k_\delta}{k_\delta\left[MT_P s^2 + (M + DT_P)\, s + D\right]} \tag{33}$$

where $k_\delta = 1.5V_n^2/X_g$, and T_P is a time constant.

Subsequently, the VSG reactive power control is reconstructed as

$$Q^* G_{RFQ}(s) + (Q^* - Q)\left(k_{Qp} + k_{Qi}/s\right) + V_n = V^* \tag{34}$$

where $G_{RFQ}(s)$ denotes a feedforward controller. k_{Qp} and k_{Qi} denote proportional and integral control coefficients. V_n and V^* denote the nominal voltage and the VSG's voltage set point, respectively.

Similarly, $G_{RFQ}(s)$ is obtained by assuming that (15) becomes the system as $1/(T_Q s+1)$ when the coupling effect is disregarded and the feedforward controller $G_{RFQ}(s)$ is applied. From (15) and (34), $G_{RFQ}(s)$ is derived as

$$G_{RFQ} = \frac{l_0}{(T_Q s+1)} - k_{Qp} \tag{35}$$

where $l_0 = 1/k_V + k_{Qp} - T_Q k_{Qi}$ and $k_V = 1.5V_n/X_g$.

In addition, the current-voltage control is applied as

$$\left(\boldsymbol{i}_f^* - \boldsymbol{i}_f\right)\left(k_{ip} + k_{ii}/s\right) + j\omega_0 L_f \boldsymbol{i}_f + \boldsymbol{v}_f = \boldsymbol{v}_o^*, \tag{36}$$

$$\left(\boldsymbol{v}_f^* - \boldsymbol{v}_f\right)\left(k_{vp} + k_{vi}/s\right) + j\omega_0 C_f \boldsymbol{v}_f = \boldsymbol{i}_f^* \tag{37}$$

where k_{ip} and k_{ii} denote the proportional and the integral controller gains for the converter-side current control, and k_{vp} and k_{vi} denote the corresponding control coefficients for the capacitor voltage control.

The virtual impedance is involved in the VSG as

$$v_{vir}^* = \boldsymbol{i}_g\left(R_{vir} + jX_{vir}\right) = \boldsymbol{i}_g \boldsymbol{Z}_{vir} \tag{38}$$

where v_{vir}^* denotes the extra voltage which is introduced by the virtual impedance. R_{vir} and X_{vir} denote virtual resistance and inductance, respectively.

2.2 Small-Signal Model Derivation

The interconnection circuit is firstly formulated as

$$\Delta\dot{\mathbf{x}}_{sys} = \mathbf{A}_{sys}\Delta\mathbf{x}_{sys} + \mathbf{B}_{sys}^{\omega}\Delta\omega_m + \mathbf{B}_{sys}^{o}\Delta\boldsymbol{v}_o + \mathbf{B}_{sys}^{g}\Delta\boldsymbol{v}_g \tag{39}$$

where the state vector is $\Delta\mathbf{x}_{sys} = [\Delta\boldsymbol{i}_f \ \Delta\boldsymbol{v}_f \ \Delta\boldsymbol{i}_g]^{\mathrm{T}}$, and the system matrices $\mathbf{A}_{sys}$, $\mathbf{B}_{sys}^{\omega}$, $\mathbf{B}_{sys}^{o}$ and $\mathbf{B}_{sys}^{g}$ are formulated as follows:

$$\mathbf{A}_{sys} = \begin{bmatrix} -\frac{R_f}{L_f} - j\omega_{m0} & -\frac{1}{L_f} & 0 \\ \frac{1}{C_f} & -j\omega_{m0} & -\frac{1}{C_f} \\ 0 & \frac{1}{L_g} & -\frac{R_g}{L_g} - j\omega_{m0} \end{bmatrix},$$

$$\mathbf{B}_{sys}^{\omega} = -j\left[\boldsymbol{i}_{f0} \ \boldsymbol{v}_{f0} \ \boldsymbol{i}_{g0}\right]^{\mathrm{T}}, \mathbf{B}_{sys}^{o} = \left[\frac{1}{L_f} \ 0 \ 0\right]^{\mathrm{T}}, \mathbf{B}_{sys}^{g} = -\left[0 \ 0 \ \frac{1}{L_g}\right]^{\mathrm{T}}$$

where ω_{m0}, $\boldsymbol{i}_{f0}$, $\boldsymbol{v}_{f0}$, and $\boldsymbol{i}_{g0}$ denote state variables on the equilibrium point.

In (39), the grid-voltage perturbation $\Delta\boldsymbol{v}_g$ can be formulated as

$$\Delta\boldsymbol{v}_g = V_n\left[\cos\delta_0 - \cos\left(\delta_0 + \Delta\theta_m\right)\right] + jV_n\left[\sin\delta_0 - \sin\left(\delta_0 + \Delta\theta_m\right)\right]. \tag{40}$$

To linearize the sinusoidal terms, $\cos\Delta\theta_m$ and $\sin\Delta\theta_m$ are written as

$$\cos\Delta\theta_m = \underbrace{\frac{\cos\delta_{max} - \cos\delta_0}{\delta_{max} - \delta_0}}_{a_{cos}}\Delta\theta_m + 1,\ \sin\Delta\theta_m = \underbrace{\frac{\sin\delta_{max} - \sin\delta_0}{\delta_{max} - \delta_0}}_{a_{sin}}\Delta\theta_m \quad (41)$$

Where δ_{max} is the estimated maximum angel under the small perturbation.

Substituting (41) into (40), we have

$$\Delta \boldsymbol{v}_g = -V_n\Delta\theta_m[\underbrace{(a_{cos}\cos\delta_0 - a_{sin}\sin\delta_0)}_{a_{\theta d}} + j\underbrace{(a_{cos}\sin\delta_0 + a_{sin}\cos\delta_0)}_{a_{\theta q}}]. \quad (42)$$

Additionally, the small-signal model of the power calculation is

$$\begin{aligned}\Delta P + j\Delta Q &= \frac{3}{2}\left(\Delta\boldsymbol{v}_f\bar{\boldsymbol{i}}_{g0} + \Delta\bar{\boldsymbol{i}}_g\boldsymbol{v}_{f0} + \Delta\boldsymbol{v}_f\Delta\bar{\boldsymbol{i}}_g\right)\\ &\approx \frac{3}{2}\left(\Delta\boldsymbol{v}_f\bar{\boldsymbol{i}}_{g0} + \Delta\bar{\boldsymbol{i}}_g\boldsymbol{v}_{f0}\right)\end{aligned} \quad (43)$$

where $\bar{\boldsymbol{i}}_g$ and $\bar{\boldsymbol{i}}_{g0}$ are conjugate values of $\boldsymbol{i}_g$ and $\boldsymbol{i}_{g0}$, respectively.

Moreover, from (32) and (33), the VSG active power control is formulated in the sense of small signal as

$$\Delta\dot{\mathbf{x}}_{apc} = \mathbf{A}_{apc}\Delta\mathbf{x}_{apc} + \mathbf{B}^{p}_{apc}\Delta P + \mathbf{B}^{ref}_{apc}\Delta P^* \quad (44)$$

where the state vector is $\Delta\mathbf{x}_{apc} = [\Delta\omega_s\ \Delta\theta_m\ \Delta x_{F1}\ \Delta x_{F2}]^{\mathrm{T}}$. In $\Delta\mathbf{x}_{apc}$, there are two state variables Δx_{F1} and Δx_{F2}. They are introduced by the feedforward controller $G_{RFP}(s)$. The system matrices $\mathbf{A}_{apc}$, $\mathbf{B}^{ref}_{apc}$ and $\mathbf{B}^{p}_{apc}$ are

$$\mathbf{A}_{apc} = \begin{bmatrix} -\frac{D}{M} & 0 & 0 & 0\\ 1 & 0 & 1 & 0\\ 0 & 0 & -\frac{1}{T_P} - \frac{D}{M} & 1\\ 0 & 0 & -\frac{D}{MT_P} & 0\end{bmatrix},\ \mathbf{B}^{p}_{apc} = -\left[\frac{1}{M}\ 0\ 0\ 0\right]^{\mathrm{T}},$$

$$\mathbf{B}^{ref}_{apc} = \left[0\ 0\ -\frac{2X_g}{3V_n^2T_P^2}\ \frac{3V_n^2T_P - 2DX_g}{3MV_n^2T_P^2}\right]^{\mathrm{T}}.$$

Similarly, from (34) and (35), the VSG reactive power control is formulated in the sense of small signal as

$$\Delta\dot{\mathbf{x}}_{rpc} = \mathbf{A}_{rpc}\Delta\mathbf{x}_{rpc} + \mathbf{B}^{ref}_{rpc}\Delta Q^* + \mathbf{B}^{q}_{rpc}\Delta Q \quad (45)$$

$$\Delta V^* = \mathbf{C}_{rpc}\Delta\mathbf{x}_{rpc} - k_{Qp}\Delta Q \quad (46)$$

where the state vector is $\Delta\mathbf{x}_{rpc} = [\Delta x_{V^*}\ \Delta x_{F0}]^{\mathrm{T}}$. In $\Delta\mathbf{x}_{rpc}$, Δx_{F0} is the state variable that comes from the feedforward controller $G_{RFQ}(s)$. Here, the system matrices $\mathbf{A}_{rpc}$, $\mathbf{B}^{ref}_{rpc}$, $\mathbf{B}^{q}_{rpc}$ and $\mathbf{C}_{rpc}$ are

$$\mathbf{A}_{rpc} = -\begin{bmatrix}0 & 0\\ 0 & 1\end{bmatrix}, \mathbf{B}^{ref}_{rpc} = \begin{bmatrix}1\\ l_0\end{bmatrix}, \mathbf{B}^{q}_{rpc} = -\begin{bmatrix}1\\ 0\end{bmatrix}, \mathbf{C}_{rpc} = \left[k_{Qi}\ \frac{1}{T_f}\right]^{\mathrm{T}}.$$

The virtual impedance's effect can be formulated as

$$\Delta \boldsymbol{v}_f^* = \Delta V^* - \Delta \boldsymbol{i}_g \boldsymbol{Z}_{vir} = \Delta V^* - \Delta \boldsymbol{v}_{vir}^*. \tag{47}$$

Furthermore, from (36) and (37), the model of the current-voltage regulation is formulated as

$$\Delta \boldsymbol{v}_o^* = k_{ip}\Delta\dot{\boldsymbol{\zeta}} + k_{ii}\Delta\boldsymbol{\zeta} + j\omega_0 L_f \Delta \boldsymbol{i}_f + \Delta \boldsymbol{v}_f \tag{48}$$

$$\Delta \boldsymbol{i}_f^* = k_{vp}\Delta\dot{\boldsymbol{\gamma}} + k_{vi}\Delta\boldsymbol{\gamma} + j\omega_0 C_f \Delta \boldsymbol{v}_f \tag{49}$$

where $\Delta\boldsymbol{\zeta}$ and $\Delta\gamma$ are two state variables as follows:

$$\Delta\dot{\boldsymbol{\zeta}} = \Delta \boldsymbol{i}_f^* - \Delta \boldsymbol{i}_f,\ \Delta\dot{\boldsymbol{\gamma}} = \Delta \boldsymbol{v}_f^* - \Delta \boldsymbol{v}_f. \tag{50}$$

Finally, the effect of the control latency $e^{-T_d s}$ is considered as

$$\Delta \boldsymbol{v}_o \approx \frac{1}{T_d s + 1} \Delta \boldsymbol{v}_o^*. \tag{51}$$

For a comprehensive small-signal modeling, the shift of the equilibrium point should be considered as well. Illustrating by Fig. 27, in the case that the VSG output is fixed, the static state variables can be directly calculated by using the real and virtual impedance.

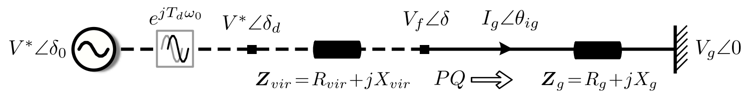

Fig. 27: The static phasor representation.

To calculate the steady-state variables, assuming the VSG output power is the equal to the set point, i.e., $P = P^*$ and $Q = Q^*$, which leads to

$$P^* + jQ^* = \frac{3}{2} V_f \angle \delta I_g \angle - \theta_{ig} = \frac{3}{2} \frac{V_f^2 e^{j\theta_{zg}} - V_f V_g e^{j\left(\theta_{zg}+\delta\right)}}{\|\boldsymbol{Z}_g\|} \tag{52}$$

where θ_{zg} represents the angle shift that comes from the grid impedance $\boldsymbol{Z}_g$. Approximately, $e^{j\delta} \approx 1 + j\delta$, and $V_g \approx V_n$. Then, from (52), we have

$$\frac{2\|\boldsymbol{Z}_g\|P^*}{3} = V_f^2 \cos\theta_{zg} - V_f V_n \left(\cos\theta_{zg} - \delta \sin\theta_{zg}\right) \tag{53}$$

$$\frac{2\|\boldsymbol{Z}_g\|Q^*}{3} = V_f^2 \sin\theta_{zg} - V_f V_n \left(\delta\cos\theta_{zg} + \sin\theta_{zg}\right) \tag{54}$$

From (53) and (54), V_f and δ can be written as

$$V_f = \frac{V_n}{2} + \sqrt{\frac{V_n^2}{4} + \frac{2}{3}\|\boldsymbol{Z}_g\| \left(P^* \cos\theta_{zg} + Q^* \sin\theta_{zg}\right)} \tag{55}$$

$$\delta = \frac{\cos\theta_{zg}}{\sin\theta_{zg}} \left(1 - \frac{V_f}{V_n}\right) + \frac{2\|\boldsymbol{Z}_g\|P^*}{3V_f V_n \sin\theta_{zg}} \tag{56}$$

Using (55) and(56), the grid current $I_g e^{j\theta_{ig}}$ is expressed as

$$I_g e^{j\theta_{ig}} = \frac{V_g e^{j(\delta-\theta_{zg})} - V_n e^{-j\theta_{zg}}}{\|\boldsymbol{Z}_g\|}. \tag{57}$$

Subsequently, $V^* e^{j\delta_d}$ is derived as

$$V^* e^{j\delta_d} = V_f e^{j\delta} + I_g e^{j\theta_{ig}} \|\boldsymbol{Z}_{vir}\| e^{j\theta_{zvir}} \tag{58}$$

where δ_d denotes the VSG output voltage angle, and θ_{zvir} is the angle shift that comes from the virtual impedance. Then, from (58), $V^* e^{j\delta_0}$ is obtained as

$$V^* e^{j\delta_0} = V^* e^{j\delta_d - T_d\omega_0}. \tag{59}$$

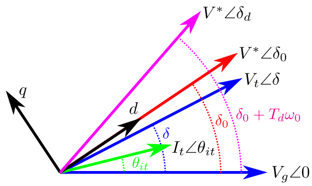

Fig. 28: The relationship among the phasors.

The relationship among the phasors is presented in Fig. 28. From it, $\boldsymbol{i}_{g0}$, $\boldsymbol{v}_{f0}$, and $\boldsymbol{i}_{f0}$ are calculated as

$$\boldsymbol{i}_{g0} = I_g e^{j\left(\theta_{ig}-\delta_0\right)}, \boldsymbol{v}_{f0} = V_f e^{j(\delta-\delta_0)}, \boldsymbol{i}_{f0} = i_{gd0} + j\left(i_{gq0} + V_n\omega_0 C_f\right). \tag{60}$$

Combining the small-signal models and the initial variable calculation, the complete model is derived as

$$\Delta\dot{\mathbf{x}} = \underbrace{\begin{bmatrix} \mathbf{A}_{11} & \mathbf{A}_{12} \\ \mathbf{0} & \mathbf{A}_{22} \end{bmatrix}}_{\mathbf{A}} \Delta\mathbf{x} + \mathbf{B} \underbrace{\begin{bmatrix} \Delta P^* \\ \Delta Q^* \end{bmatrix}}_{\Delta\mathbf{U}} \tag{61}$$

where the sate vector is $\Delta\mathbf{x} = [\Delta\mathbf{x}_{sys}\ \Delta\boldsymbol{v}_o\ \Delta\boldsymbol{\zeta}\ \Delta\gamma\ \Delta x_{V^*}\ \Delta\omega_s\ \Delta\theta_m\ \Delta x_{F0}\ \Delta x_{F1}\ \Delta x_{F2}]^T$, and the system matrices are

$$\underbrace{\begin{bmatrix} -\frac{1}{T_f} & 0 & 0 \\ 0 & -\frac{1}{T_P} - \frac{D}{M} & 1 \\ 0 & -\frac{D}{MT_P} & 0 \end{bmatrix}}_{\mathbf{A}_{22}}, \underbrace{\begin{bmatrix} 0 & 0 & 0 & 0 & 0 & 0 & \frac{k_{vp}k_{ip}}{T_d} & 0\,0\,0\,1\,0\,0\,0\,0 \\ i_{fq0} & -i_{fd0} & v_{fq0} & -v_{fd0} & i_{fq0} & -i_{fd0} & 0 & 0\,0\,0\,0\,0\,0\,0\,1 \\ 0 & 0 & 0 & 0 & 0 & 0 & 0 & 0\,0\,0\,0\,0\,0\,0\,0 \end{bmatrix}^{\mathrm{T}}}_{\mathbf{A}_{12}},$$

$$
\underbrace{\begin{bmatrix}
\frac{-R_f}{L_f} & \omega_0 & \frac{-1}{L_f} & 0 & 0 & 0 & \frac{1}{L_f} & 0 & 0 & 0 & 0 & 0 & 0 & i_{fq0} & 0 \\
-\omega_0 & \frac{-R_f}{L_f} & 0 & \frac{-1}{L_f} & 0 & 0 & 0 & \frac{1}{L_f} & 0 & 0 & 0 & 0 & 0 & -i_{fd0} & 0 \\
\frac{1}{C_f} & 0 & 0 & \omega_0 & \frac{-1}{C_f} & 0 & 0 & 0 & 0 & 0 & 0 & 0 & 0 & v_{fq0} & 0 \\
0 & \frac{1}{C_f} & -\omega_0 & 0 & 0 & \frac{-1}{C_f} & 0 & 0 & 0 & 0 & 0 & 0 & 0 & -v_{fd0} & 0 \\
0 & 0 & \frac{1}{L_g} & 0 & \frac{-R_g}{L_g} & \omega_0 & 0 & 0 & 0 & 0 & 0 & 0 & 0 & i_{gq0} & \frac{a_{\theta d} V_n}{L_g} \\
0 & 0 & 0 & \frac{1}{L_g} & -\omega_0 & -\frac{R_g}{L_g} & 0 & 0 & 0 & 0 & 0 & 0 & 0 & -i_{gd0} & \frac{a_{\theta q} V_n}{L_g} \\
\frac{-k_{ip}}{T_d} & \frac{-\omega_0 L_f}{T_d} & \frac{a_{vtd} k_{vp} k_{ip}+1}{T_d} & \frac{a_{vtq} k_{vp} k_{ip}}{T_d} & \frac{a_{itd} k_{vp} k_{ip}}{T_d} & \frac{a_{itq} k_{vp} k_{ip}}{T_d} & \frac{-1}{T_d} & 0 & \frac{k_{ii}}{T_d} & 0 & \frac{k_{vi} k_{ip}}{T_d} & 0 & \frac{k_{Qi} k_{vp} k_{ip}}{T_d} & 0 & 0 \\
\frac{\omega_0 L_f}{T_d} & \frac{-k_{ip}}{T_d} & \frac{\omega_0 C_f k_{ip}}{T_d} & \frac{-k_{vp} k_{ip}+1}{T_d} & \frac{-\omega_0 L_{vir} k_{vp} k_{ip}}{T_d} & \frac{-R_{vir} k_{vp} k_{ip}}{T_d} & 0 & \frac{-1}{T_d} & 0 & \frac{k_{ii}}{T_d} & 0 & \frac{k_{vi} k_{ip}}{T_d} & 0 & 0 & 0 \\
-1 & 0 & a_{vtd} k_{vp} & a_{vtq} k_{vp} & a_{itd} k_{vp} & a_{itq} k_{vp} & 0 & 0 & 0 & 0 & k_{vi} & 0 & k_{Qi} k_{vp} & 0 & 0 \\
0 & -1 & \omega_0 C_f & -k_{vp} & -\omega_0 L_{vir} k_{vp} & -R_{vir} k_{vp} & 0 & 0 & 0 & 0 & 0 & k_{vi} & 0 & 0 & 0 \\
0 & 0 & a_{vtd} & a_{vtq}+\frac{\omega_0 C_f}{k_{vp}} & a_{itd} & a_{itq} & 0 & 0 & 0 & 0 & 0 & 0 & k_{Qi} & 0 & 0 \\
0 & 0 & 0 & -1 & -\omega_0 L_{vir} & -R_{vir} & 0 & 0 & 0 & 0 & 0 & 0 & 0 & 0 & 0 \\
0 & 0 & \frac{3 i_{gq0}}{2} & \frac{-3 i_{gd0}}{2} & \frac{-3 v_{fq0}}{2} & \frac{3 v_{fd0}}{2} & 0 & 0 & 0 & 0 & 0 & 0 & 0 & 0 & 0 \\
0 & 0 & \frac{-3 i_{gd0}}{2M} & \frac{-3 i_{gq0}}{2M} & \frac{-3 v_{fd0}}{2M} & \frac{-3 v_{fq0}}{2M} & 0 & 0 & 0 & 0 & 0 & 0 & 0 & \frac{-D}{M} & 0 \\
0 & 0 & 0 & 0 & 0 & 0 & 0 & 0 & 0 & 0 & 0 & 0 & 0 & 1 & 0
\end{bmatrix}}_{\mathbf{A}_{11}},
$$

$$\underbrace{\begin{bmatrix} 0&0&0&0&0&0&0&0&0&0&0&0&0&0&0&0&\frac{-2X_g}{3V_n^2T_P^2}&\frac{3V_n^2T_P-2DX_g}{3MV_n^2T_P^2} \\ 0&0&0&0&0&0&0&0&0&0&0&0&1&0&0&\frac{l_0}{T_f}&0&0 \end{bmatrix}}_{\mathbf{B}}. \tag{62}$$

3 Development of the Stability-Oriented Optimal VSG Tuning

To develop the stability-oriented VSG tuning, the complete model obtained in the previous section is firstly validated and analyzed in this section. For this, the settings used in the validation are presented in Table 4. Then, the grid-tied VSG depicted in Fig. 26 is implemented in Digsilent, and the small-signal model as (61) is realized in Matlab. As depicted in Fig. 29, there is an accurate correspondence between the power perturbations (ΔP and ΔQ under the set point changes) generated from the developed small-signal model and that obtained from the simulation.

Table 4: System settings for the stability-oriented optimal VSG tuning

Variable	Values	Variable	Values	Variable	Values	Variable	Values
S_{base}	1 MVA	V_n	$690\sqrt{2/3}$ V	L_f	0.12 pu	R_f	0.006 pu
L_g	0.14 pu	R_g	0.014 pu	C_f	0.2 pu	T_d	0.00075 s
k_{ip}	0.27 pu	k_{ii}	31.5 pu	k_{vp}	0.07 pu	k_{vi}	12 pu
X_{vir}	1.2 pu	R_{vir}	0.12 pu	k_{Qp}	0.24 pu	k_{Qi}	6.5 pu
H	15 s	D	50 pu	T_P	0.5 s	T_Q	0.5 s

Base values: V_n/S_{base} (k_{Qp} and k_{Qi}), ω_0/S_{base} (D), $1.5V_n^2/S_{base}$ (k_{ip} and k_{ii}) and $S_{base}/1.5V_n^2$ (k_{vp} and k_{vi}).

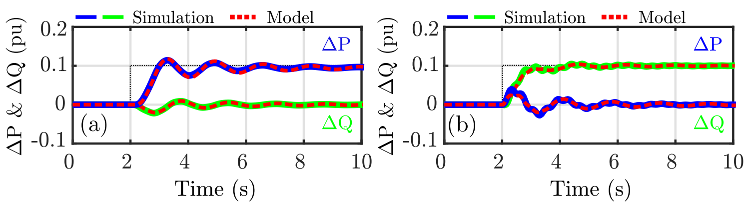

Fig. 29: Small-signal model validation. (a) $\Delta P^* = 0.1$ pu; (b) $\Delta Q^* = 0.1$ pu.

Subsequently, using the same system settings, the eigenvalues of the derived model presented in Table 5.

Table 5: System eigenvalues

$\lambda_{1,2}$	$-392 \pm 3070j$	$\lambda_{3,4}$	$-379 \pm 2419j$	$\lambda_{5,6}$	$-308 \pm 730j$
$\lambda_{7,8}$	$-171 \pm 471j$	$\lambda_{9,10}$	$-128 \pm 15.42j$	$\lambda_{11,12}$	$-0.85 \pm 16.23j$
$\lambda_{13,14}$	$-0.35 \pm 3.89j$	λ_{15}	-4.55	λ_{16}	-1.67
λ_{17}	-2	λ_{18}	-2		

Here, the eigenvalues λ_{16}, λ_{17}, and λ_{18} are introduced by the feedforward controllers $G_{RFP}(s)$ and $G_{RFQ}(s)$. From (33) and (35), it is clear that they correspond to $-D/M$, $1/T_P$, and $1/T_Q$, respectively.

Table 6: The eigenvalue sensitivities

$\frac{\partial \lambda_{17}}{\partial T_P}$	$4 \pm 0j$	$\frac{\partial \lambda_1}{\partial T_P}, \frac{\partial \lambda_2}{\partial T_P}, \ldots, \frac{\partial \lambda_{16}}{\partial T_P}$ and $\frac{\partial \lambda_{18}}{\partial T_P}$	$0 \pm 0j$
$\frac{\partial \lambda_{18}}{\partial T_Q}$	$4 \pm 0j$	$\frac{\partial \lambda_1}{\partial T_Q}, \frac{\partial \lambda_2}{\partial T_Q}, \ldots, \frac{\partial \lambda_{16}}{\partial T_Q}$ and $\frac{\partial \lambda_{17}}{\partial T_Q}$	$0 \pm 0j$

To assess the feedforward control coefficients' impact on the other system eigenvalues, i.e., λ_1 to λ_{15}, the eigenvalue sensitivities are calculated and presented in Table 6. It is clear that T_P and T_Q only affect the eigenvalues λ_{16} and λ_{17}. In this manner, for the stability-oriented optimal VSG tuning, the eigenvalues λ_1 to λ_{15} can be firstly tuned to extend the stability boundary, and λ_{16} and λ_{17} are used to modify the power control dynamic as they are always stable when T_P and T_Q are greater than zero.

3.1 First-Step Optimization

As discussed above, in the first-step optimization, the main objective is guaranteeing that the control stability is always fulfilled. In another word, all the eigenvalues locate should have a negative real part, which can be written as

$$\forall \lambda_i \; i \in \{1, 2, ..., I\} \;\; Re\,(\lambda_i) < 0 \tag{63}$$

where λ_i is the system eigenvalue, and I is the the matrix $\mathbf{A}_{11}$ dimension.

In (63), all the eigenvalues are considered without any ranking; however, it is better to let the eigenvalues, which are sensitive to the parameter changes, e.g., grid impedance change, stay away from the imaginary axis. For this, an objective function is defined as follows:

$$J_1(\mathbf{k}_1) = \sum_{i=1}^{I} \frac{w_i}{|Re\,(\lambda_i)|} \tag{64}$$

where $\mathbf{k}_1 = [k_{ip}\; k_{ii}\; k_{vp}\; k_{vi}\; R_{vir}\; L_{vir}\; k_{Qp}\; k_{Qi}]^{\mathrm{T}}$ is a set of VSG control parameters. w_i is the weighting factor for ranking the eigenvalues, and it is

$$w_i = \begin{cases} 1, & Re\left(\partial\lambda_i/\partial L_g\right) \leq 0, \\ w_1, & 0 < Re\left(\partial\lambda_i/\partial L_g\right) \leq s_t, \\ w_2, & s_t < Re\left(\partial\lambda_i/\partial L_g\right). \end{cases} \tag{65}$$

where w_1, w_2, and s_t represent the weighting factors and the threshold.

From (64), the first-step optimization is formulated as

$$\begin{array}{ll} \min & J_1(\mathbf{k}_1) \\ s.t. & \mathbf{k}_{1min} \leq \mathbf{k}_1 \leq \mathbf{k}_{1max},\ \zeta_{min} \leq \zeta_i \end{array} \tag{66}$$

where $\mathbf{k}_{1min}$ and $\mathbf{k}_{1max}$ denote the parameter constraints. ζ_i is the damping ratio of each eigenvalue, and ζ_{min} denotes the damping ratio constraint.

3.2 Second-Step Optimization

After the first-step optimization, the control stability is ensured. Then, the power control dynamic is considered in this stage of optimization. Using the time-integral criteria, the objective function is defined as

$$J_2(\mathbf{k}_2) = \varepsilon_1 \int_0^T t\,|P^* - P|\,dt + \varepsilon_2 \int_0^T t\,|Q^* - Q|\,dt \tag{67}$$

where $\mathbf{k}_2 = [T_P\ T_Q]$ is a set of feedforward control coefficients. T denotes the time period for evaluating the objective function $J_2(\mathbf{k}_2)$. ε_1 and ε_2 represent two weighting factors.

The second-step optimization is then formulated as

$$\begin{array}{ll} \min & J_2(\mathbf{k}_2) \\ s.t. & \mathbf{k}_{2min} \leq \mathbf{k}_2 \leq \mathbf{k}_{2max} \end{array} \tag{68}$$

where $\mathbf{k}_{2min}$ and $\mathbf{k}_{2max}$ are parameter constraints.

3.3 Implementation Using the Particle Swarm Optimization

As the particle swarm optimization (PSO) provides an easy implementation to solve the objective functions with the stochastic nature, it is used here for realizing the proposed tuning algorithm [86]. The corresponding flowchart is shown in Fig. 30, and the implementation details are presented as follows:

1) The system settings, i.e., S_{base}, R_f, L_f, C_f, R_g, L_g, T_s, M and D, are firstly initialized. In practice, they can be detected and updated online.

2) The constraints and weighting factors, i.e., $\mathbf{k}_{1min}$, $\mathbf{k}_{1max}$, ζ_{min}, s_t, w_1 and w_2, are initialized for the first-step optimization. $\mathbf{k}_{1min}$ and $\mathbf{k}_{1max}$ are set according to the conventional bandwidth criteria [38, 71, 87]. s_t, w_1 and w_2 are set to $1e3$, 10 and $3e3$ for the optimization.

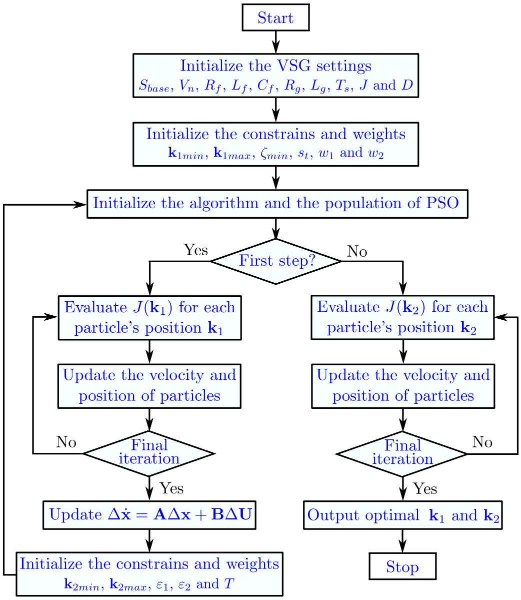

Fig. 30: Flowchart of the proposed tuning algorithm.

3) Initialize the PSO. Specifically, the population size N_p is 50, the inertia coefficient ω_p is set to 0.73, the acceleration coefficients c_{p1} and c_{p2} are set to 1.5, the velocity limitations $\mathbf{v}_{p1}$ and $\mathbf{v}_{p2}$ are set to $0.5(\mathbf{k}_{1max} - \mathbf{k}_{1min})$ and $0.5(\mathbf{k}_{2max} - \mathbf{k}_{2min})$, and the iteration number N_I is 300.

4) Calculate $J(\mathbf{k}_1)$ or $J(\mathbf{k}_2)$ according to each particle's position and update the particles following the classical PSO rules [88].

5) If the iterations are not complete, go to 4). When the iterations and the first-step optimization are completed, go to 6). Otherwise, two steps of the tuning are completed, the optimal solutions $\mathbf{k}_1$ and $\mathbf{k}_2$ are solved.

6) Update (61) with the first-step optimization solution $\mathbf{k}_1$. Initialize the constraints and weighting factors, i.e., $\mathbf{k}_{2min}$, $\mathbf{k}_{2max}$, ε_1, ε_2 and T, for the second-step optimization. Here, $\mathbf{k}_{2min}$ and $\mathbf{k}_{2max}$ can be set according to the first-order plant response [89]. ε_1 and ε_2 are 0.5, and T is 5 s. After the internalization for the second-step optimization, go to 3).

4 Simulation Validations

For the validation of the proposed method, a 10-bus test system as Fig. 31 is implemented in Digsilent. This test system can be considered as a modification based on the classical three-machine infinite-bus model in [90], where the

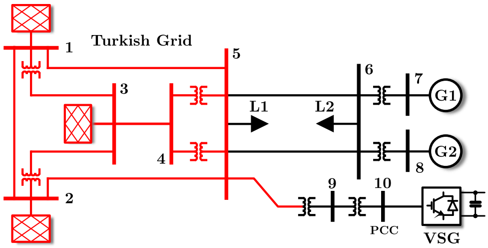

Fig. 31: Diagram of the test system in Digsilent.

infinite bus is replaced with a equivalent grid model of a part of the Turkish grid. To validate the proposed strategies under different short-circuit ratios (SCRs), the grid impedance $\boldsymbol{Z}_g$ is modified to let SCR vary from 3 to 11 [36]. Correspondingly, the optimal VSG control parameters are generated by the optimal tuning algorithm in Matlab.

Firstly, the conventional VSG without the proposed control scheme and VSG tuning algorithm is validated. Using the parameters given in Table 4, the VSG responses under the active power and reactive power set point changes (P^* steps from 0.9 pu to 1 pu, and Q^* steps from 0 pu to 0.1 pu) are shown in Fig. 32. In the case that the SCR increases from 3 to 11, the VSG becomes more oscillatory, which indicates that the overall damping level is decreasing and the stability margin is restricted.

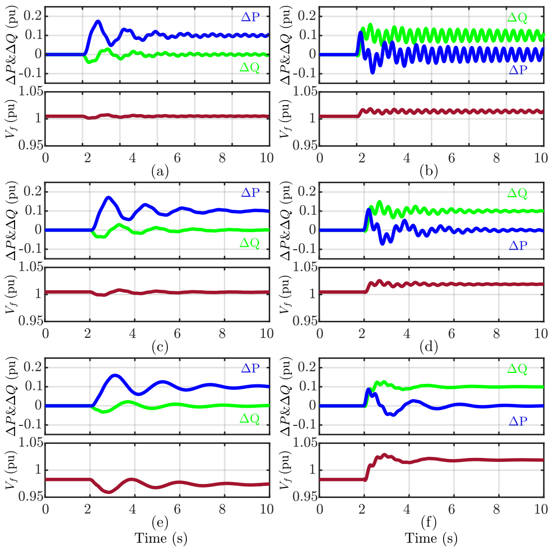

Fig. 32: VSG without the optimization. $SCR = 11$: (a) P^* steps; (b) Q^* power steps; $SCR = 7$: (c) P^* steps; (d) Q^* steps; $SCR = 3$: (e) P^* steps; (f) Q^* steps.

Subsequently, the first-step optimization is applied, and the simulation results under the same scenario are shown in Fig. 33. Compared with the VSG without the optimal tuning, the VSG with the first-step optimal tuning tends to be less oscillatory when the SCR increases from 3 to 11. From the dominant eigenvalue comparison in Fig. 34, the first-step optimization removes the eigenvalues that are sensitive to grid-impedance change. In this way, the VSG control stability is enhanced.

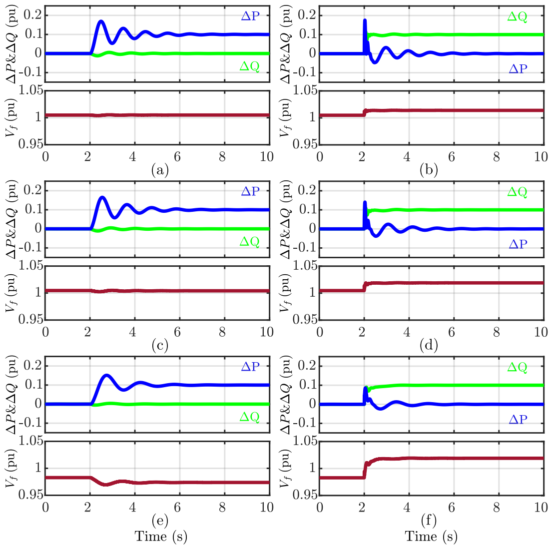

Fig. 33: VSG with the first-step optimization. $SCR = 11$: (a) P^* steps; (b) Q^* power steps; $SCR = 7$: (c) P^* steps; (d) Q^* steps; $SCR = 3$: (e) P^* steps; (f) Q^* steps.

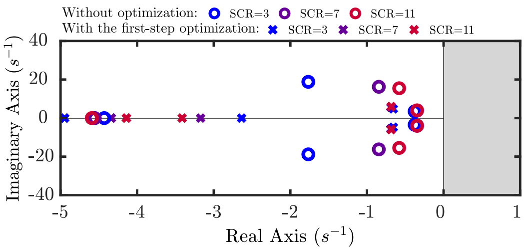

Fig. 34: The dominant eigenvalue comparison.

However, the power oscillations cased by the synthetic inertia as well as the coupling effect still exist. To alleviate these oscillations, the second-step optimal tuning is applied to generate the optimal feedforward control parameters. As depicted in Fig. 35, with the help of the feedforward controllers and the second-step optimal tuning, the original power oscillations are significantly attenuated.

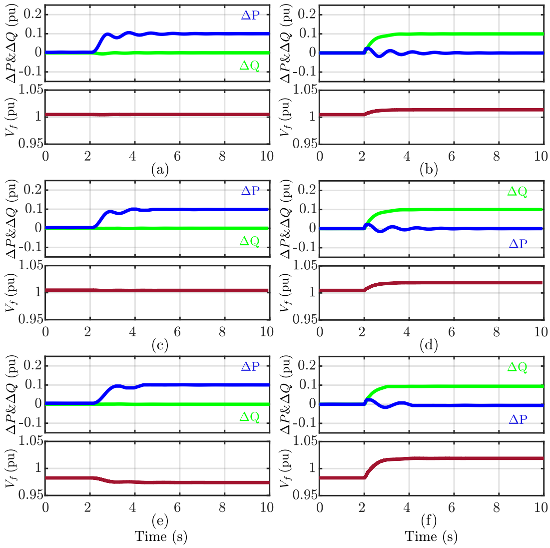

Fig. 35: VSG with the two-step optimization. $SCR = 11$: (a) P^* steps; (b) Q^* power steps; $SCR = 7$: (c) P^* steps; (d) Q^* steps; $SCR = 3$: (e) P^* steps; (f) Q^* steps.

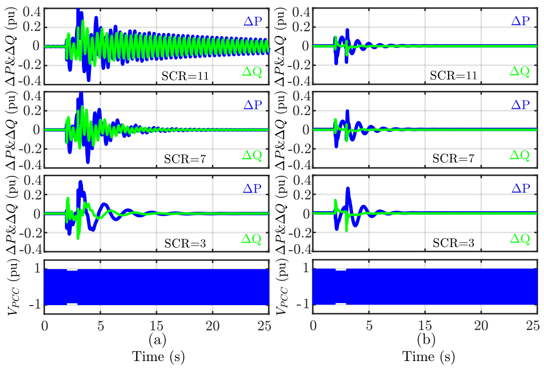

Fig. 36: VSG under the symmetrical voltage sags. (a) Without optimization; (b) With the proposed feedforward filters and optimization algorithm

Moreover, the proposed method is validated under the symmetrical voltage sags as well. In the simulation, the symmetrical short-circuit fault is generated to let the PCC voltage decrease to 80% of the nominal voltage level. The symmetrical fault is cleared after 1 s. As depicted in Fig. 36, using the optimal VSG tuning, the transients are less intense when the fault happens. Moreover, when the fault is removed, it takes less time to recover the original operation status.

5 Summary

In this chapter, a VSG control scheme, which contains two feedforward controllers for the VSG power control, is firstly proposed. Subsequently, its full-order model is derived on the basis of the state-space representation. Involving the impacts of the inner current-voltage regulation, virtual impedance, latency, and shift of the equilibrium point, the derived small-signal model provides sufficient accuracy for the VSG parameter tuning algorithm development. Afterwards, using the derived model, a two-step optimal VSG tuning algorithm is developed. Specifically, the first-step optimization is designed for improving the VSG control stability, and the second-step optimization is proposed for adjusting the VSG power control dynamic. Via the simulation validations under different operating conditions, the improvements made in extending the VSG stability boundary and improving the power control dynamic is verified.

Chapter 5. Active Damping for the Parallel Operation of Multiple Grid-Tied VSGs

1 Introduction

In the existing works on the VSG active damping control, the investigations are mainly made for a single unit, whereas the characteristic of the parallel operation of multiple grid-tied VSGs are disregarded. In this manner, when a multi-VSG system is implemented, for example, a VSG-based microgrid, the feasibility of these active damping control methods may be degraded. Considering this, the investigation on the multi-VSG system operation has gained a large popularity in recent years. For instance, in [95], the control stability and the damping effect of a multi-VSG microgrid were attained by

Table 7: Technical Features of Existing Active Damping Methods

Reference	VSG	Grid-tied	Islanded	Inertia	Tuning
[36,45,66,91]	1	✓	✗	Disregarded	Manual
[64,76]	1	✓	✗	Involved	Manual
[74]	1	✓	✗	Involved	Calculation
[25,92]	1	✓	✗	Disregarded	Manual
[93]	1	✓	✗	Disregarded	Data-driven
[94]	1	✗	✓	Involved	Manual
[95]	3	✗	✓	Disregarded	Optimization
[96]	2	✗	✓	Involved	Manual
[67,68]	2	✗	✓	Involved	Manual
[97]	4	✗	✓	Involved	Manual
[97]	4	✗	✓	Involved	Manual
[98]	3	✓	✗	Disregarded	Optimization

the control parameter optimization. An inertia control strategy was proposed in [96] for realizing the smooth transient of a multi-VSG microgrid. Moreover, in [67,68,97,97], active power control law modifications were developed for the damping of the VSG-based microgrid. A comparison of these works is given in Table 7, it is clear that these investigations were mainly made for the islanded operation mode, whereas the grid-tied case was disregarded. Only the work in [98] gives an active damping solution for the multiple grid-tied VSGs. Nevertheless, the active damping control and its tuning algorithm presented in [98] show a great complexity which needs the help of heuristic algorithms. Therefore, developing an active damping strategy which provides sufficient damping effects and a practical tuning becomes a challenge in this field. To tackle this challenge, an active damping strategy which consists of self and mutual active damping controllers is proposed.

2 Modeling of the VSG Based on the State-Space Representation and Jacobian Matrix Calculation

2.1 System Description

A schematic of multiple grid-tied VSGs is depicted in Fig. 37. Here, the boldface letters are adopted to denote complex vectors. In nth VSG's and grid's $\alpha\beta$ frames ($n = 1, 2, \ldots, N$), current and voltage vectors are written with the superscript s, for example, $\boldsymbol{v}^s_{on}$, $\boldsymbol{i}^s_{fn}$, $\boldsymbol{v}^s_{fn}$, $\boldsymbol{i}^s_{ln}$, $\boldsymbol{v}^s_{pcc}$, $\boldsymbol{i}^s_g$ and $\boldsymbol{v}^s_g$. Correspondingly, those vectors in the nth VSG's and grid's dq frames are denoted without the superscript, such as $\boldsymbol{v}_{on}$, $\boldsymbol{i}_{fn}$, $\boldsymbol{v}_{fn}$, $\boldsymbol{i}_{ln}$, $\boldsymbol{v}_{pccn}$, $\boldsymbol{I}_{ln}$, $\boldsymbol{V}_{pcc}$, $\boldsymbol{I}_g$ and $\boldsymbol{V}_g$. In addition, R_{fn}, L_{fn}, and C_{fn} are resistance, inductance, and capacitance of the inverter output filter. R_{ln} and L_{ln} denote the equivalent resistance and inductance of the lines or cables between the inverter output filter and the PCC. Regarding the external grid, its topology is disregarded, and the line impedance is simplified by the resistance R_g and inductance L_g.

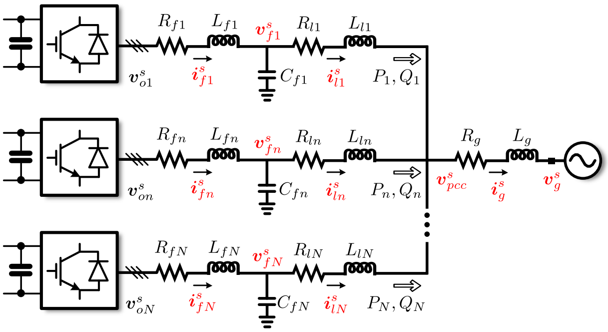

Fig. 37: Multiple parallel grid-tied VSGs.

2.2 Small-Signal Model Derivation

The passive filter and the impedance between the inverter and the PCC can be modeled in the nth VSG's dq frame as

$$L_{fn}\dot{\boldsymbol{i}}_{fn} = \boldsymbol{v}_{on} - \left(R_{fn} + j\omega_n L_{fn}\right)\boldsymbol{i}_{fn} - \boldsymbol{v}_{fn} \tag{69}$$

$$C_{fn}\dot{\boldsymbol{v}}_{fn} = \boldsymbol{i}_{fn} - j\omega_n C_{fn}\boldsymbol{v}_{fn} - \boldsymbol{i}_{ln} \tag{70}$$

$$L_{ln}\dot{\boldsymbol{i}}_{ln} = \boldsymbol{v}_{fn} - \left(R_{ln} + j\omega_n L_{ln}\right)\boldsymbol{i}_{ln} - \boldsymbol{v}_{pccn} \tag{71}$$

where ω_n represents the nth VSG's angular frequency.

For modeling multiple VSGs simultaneously, a common frame is essential. Considering this, the external grid's DQ frame is used as the common frame, and its angular frequency ω_g is assumed to be constant. Then, the angle δ_n between the nth VSG's and grid's frames is written as

$$\delta_n = \theta_n - \theta_g \tag{72}$$

where $\dot{\theta}_n = \omega_n$ and $\dot{\theta}_g = \omega_g$.

From (72), the transformations between the nth VSG's dq and grid's DQ frames are defined as

$$\boldsymbol{v}_{pccn} = e^{-j\delta_n}\boldsymbol{V}_{pcc}, \;\; \boldsymbol{I}_{ln} = e^{j\delta_n}\boldsymbol{i}_{ln}. \tag{73}$$

The dynamic of the interconnection of the PCC and the external grid is modeled in the DQ frame as

$$L_g\dot{\boldsymbol{I}}_g = \boldsymbol{V}_{pcc} - \left(R_g + j\omega_g L_g\right)\boldsymbol{I}_g - \boldsymbol{V}_g. \tag{74}$$

The VSG control schematic is shown in Fig. 38, where the nth VSG's active power control (APC) is written as

$$M_n\dot{\omega}_n = P_n^* - P_n - D_n\left(\omega_n - \omega_0\right) \tag{75}$$

where P_n^* and P_n are active power set point and feedback. M_n is ω_0-scaled virtual inertia which is $M_n = 2H_nS_{base}/\omega_0$, where H_n is the inertial constant, and S_{base} is the inverter ratted power. D_n represents the damping constants. ω_0 denotes system's nominal angular frequency.

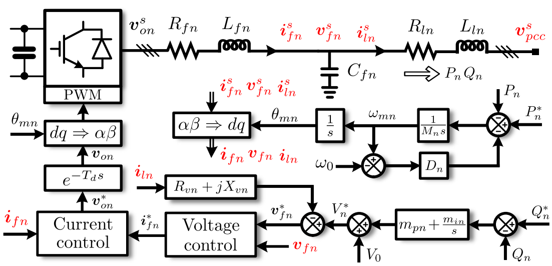

Fig. 38: Schematic of the VSG control.

The nth VSG's reactive power control (RPC) is written as

$$V_n^* = m_{pn}(Q_n^* - Q_n) + m_{in}x_{Vn} + V_0 \tag{76}$$

where Q_n^* is the reactive power set point, and Q_n is the reactive power feedback. m_{pn} and m_{in} denote the reactive-power proportional-integral control gains. V_0 is the nominal voltage, and V_n^* is the nth VSG's voltage amplitude reference. x_{Vn} is a state variable of the nth VSG's RPC, and its derivative is

$$\dot{x}_{Vn} = Q_n^* - Q_n. \tag{77}$$

The power feedback, i.e., P_n and Q_n, of the nth VSG are calculated from the grid-side current and voltage as

$$P_n + jQ_n = \frac{3}{2}\boldsymbol{v}_{fn}\bar{\boldsymbol{i}}_{ln} \tag{78}$$

where $\bar{\boldsymbol{i}}_{ln}$ is the conjugate vector of $\boldsymbol{i}_{ln}$.

The virtual impedance is applied with the current-voltage regulation as

$$\boldsymbol{v}_{fn}^* = V_n^* - \boldsymbol{i}_{ln}\left(R_{vn} + jX_{vn}\right) \tag{79}$$

where $\boldsymbol{v}_{fn}^*$ is set point fed into the inner voltage control. R_{vn} and X_{vn} denotes the virtual resistance and inductance, respectively.

The nth VSG's current-voltage control can be written in its dq frame as

$$\boldsymbol{i}_{fn}^* = k_{pn}(\boldsymbol{v}_{fn}^* - \boldsymbol{v}_{fn}) + k_{in}\boldsymbol{\gamma}_n + j\omega_n C_{fn}\boldsymbol{v}_{fn} \tag{80}$$

$$\boldsymbol{v}_{on}^* = l_{pn}(\boldsymbol{i}_{fn}^* - \boldsymbol{i}_{fn}) + l_{in}\boldsymbol{\zeta}_n + j\omega_n L_{fn}\boldsymbol{i}_{fn} + \boldsymbol{v}_{fn} \tag{81}$$

where $\boldsymbol{i}_{fn}^*$ and $\boldsymbol{v}_{on}^*$ are inverter output current and voltage references. k_{pn}, k_{in}, l_{pn}, and l_{in} denote the coefficients of the current and voltage proportional-integral controllers. $\boldsymbol{\gamma}_n$ and $\boldsymbol{\zeta}_n$ represent two state variable whose derivatives are written as

$$\dot{\boldsymbol{\gamma}}_n = \boldsymbol{v}_{fn}^* - \boldsymbol{v}_{fn},\ \dot{\boldsymbol{\zeta}}_n = \boldsymbol{i}_{fn}^* - \boldsymbol{i}_{fn}. \tag{82}$$

Here, the control latency is considered as

$$\dot{\boldsymbol{v}}_{on} \approx \frac{1}{T_d s + 1}\left(\boldsymbol{v}_{on}^* - \boldsymbol{v}_{on}\right) \tag{83}$$

where $T_d \approx 1.5T_c$, and T_c denotes the control period.

Combining (69) to (83), the system shown in Fig. 37 is represented via a group of differential equations as $\dot{\mathbf{x}} = \mathbf{f}(\mathbf{x})$. $\mathbf{f}(\mathbf{x})$ represents the vector function which can be formulated as

$$\mathbf{f}(\mathbf{x}) = \left[f_1(x_1, \ldots, x_{15N+2}) \ldots f_{15N+2}(x_1, \ldots, x_{15N+2})\right]^{\mathrm{T}} \tag{84}$$

where $f_1(x_1, \ldots, x_{15N+2})$ to $f_{15N+2}(x_1, \ldots, x_{15N+2})$ are components of $\mathbf{f}(\mathbf{x})$, and x_1 to x_{15N+2} denote state variables. The state matrix $\mathbf{x}$ is

$$\mathbf{x} = \left[\mathbf{x}_{cir1}\ \mathbf{x}_{vsg1}\ \mathbf{x}_{cir2}\ \mathbf{x}_{vsg1}\ \ldots\ \mathbf{x}_{cirN}\ \mathbf{x}_{vsgN}\ \mathbf{x}_{Ig}\right]^{\mathrm{T}} \triangleq \left[x_1\ x_2\ \ldots\ x_{15N+2}\right]^{\mathrm{T}} \quad (85)$$

where $\mathbf{x}_{cirn}$, $\mathbf{x}_{vsgn}$ and $\mathbf{x}_{Ig}$ are

$$\begin{aligned}\mathbf{x}_{cirn} &= \left[i_{fdn}\ i_{fqn}\ v_{fdn}\ v_{fqn}\ i_{ldn}\ i_{lqn}\right],\\ \mathbf{x}_{vsgn} &= \left[v_{odn}\ v_{oqn}\ \gamma_{dn}\ \gamma_{qn}\ \zeta_{dn}\ \zeta_{qn}\ x_{Vn}\ \omega_n\ \delta_n\right], \mathbf{x}_{Ig} = \left[I_{gD}\ I_{gQ}\right].\end{aligned}$$

From (84), the Jacobian matrix $\mathbf{J}$ ia calculated as

$$\mathbf{J} = \left[\frac{\partial \mathbf{f}}{\partial x_1}\ \frac{\partial \mathbf{f}}{\partial x_2}\ \cdots\ \frac{\partial \mathbf{f}}{\partial x_{15N+2}}\right]. \quad (86)$$

From $\mathbf{J}$, system eigenvalues λ_i can be solved, where $i = 1, 2, \ldots, 15N + 2$.

3 An Assessment of the Average Damping Level

In Table 8, the system settings are presented. Here, all the VSGs' interfaces with the grid are considered as the same, and the resulting SCR is around 6. The VSG control parameters are given in Table 9. Specifically, the inner current and voltage controls are adjusted to have bandwidth of 225 Hz and 135 Hz, respectively. Moreover, the virtual impedance is applied to make the equivalent impedance mainly inductive, i.e., $[\omega_0(L_g + L_{ln}) + X_{vn}] \gg (R_g + R_{ln} + R_{vn})$. The inertial constant H_n is 15 s, and the damping constant D_n

Table 8: The system settings

Variable	Values	Variable	Values	Variable	Values
S_{basen}	1 MVA	V_{line}	690 V	L_{fn}	0.12 pu
R_{fn}	0.006 pu	C_{fn}	0.2 pu	L_{ln}	0.1 pu
R_{ln}	0.01 pu	L_g	0.066 pu	R_g	0.007 pu

Table 9: The VSG control parameters

Variable	Values	Variable	Values	Variable	Values
l_{pn}	0.64 pu	l_{in}	38.59 pu	k_{pn}	0.25 pu
k_{in}	52.37 pu	R_{vn}	0.013 pu	X_{vn}	0.22 pu
T_c	0.0005 s	H_n	15 s	D_n	10 pu
m_{pn}	1.15 pu	m_{in}	3 pu	V_0	563 V

Base values are V_0/S_{basen} (m_{pn} and m_{in}), ω_0/S_{basen} (D_n), V_{line}^2/S_{basen} (l_{pn} and l_{in}) and S_{basen}/V_{line}^2 (k_{pn} and k_{in})

is set to enable a 10% static droop. Regarding the RPC, using the simplified model in [71], its bandwidth is adjusted to be the same as the APC. Without loss of generality, the amount of VSGs in parallel is set to 3.

Firstly, for the damping level assessment, the average damping ratio ζ_{av} is defined to reflect the system damping level as

$$\zeta_{av} = \sum_{l=1}^{L} \frac{-Real(\lambda_l)}{L\sqrt{Real(\lambda_l)^2 + Imag(\lambda_l)^2}} \tag{87}$$

where L denotes the number of the system dominant eigenvalues. Here, the dominant eigenvalues are defined as those with a real part greater than -2 and less than 0, i.e., $-2 < Real(\lambda_i) < 0$.

Then, the parameters of 3 parallel-connected VSGs are considered as the same, i.e., $H_1 = H_2 = H_3$ and $D_1 = D_2 = D_3$. Changing H_n and D_n in the range of $[5, 15]$ s and $[10, 50]$ pu, respectively, the average damping ratio ζ_{av} is calculated and shown on the $H_n - D_n$ plane as Fig. 39.

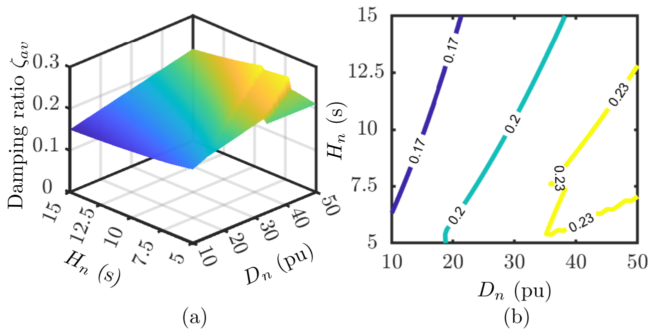

Fig. 39: Damping level assessment in the range of $H_n \in [5, 15]$ s and $D_n \in [10, 50]$ pu (a) Damping ratio ζ_{av} (b) Damping ratio contour lines.

It is clear that, the average damping ratio ζ_{av} on the entire $H_n - D_n$ plane is around 0.2 which is relatively low. Even when the damping constant D_n increases to 50 pu, the average damping ratio is still around 0.23. Then, the average damping ratio is assessed in the case that VSG's control parameters are different. For this, two VSGs' settings are firstly fixed, e.g., $H_2 = 11.25$ s, $H_3 = 15$ s, $D_2 = 15$ pu and $D_3 = 10$ pu. Afterwards, H_1 and D_1 of one VSG are changed in the range of $[5, 15]$ s and $[10, 50]$ pu. As depicted in Fig. 40, the maximum average damping ratio on the entire $H_n - D_n$ plane is around 3. Therefore, as indicated in Fig. 39 and Fig. 40, the VSGs in parallel could be poorly damped even when their inertia and damping constant settings are adjusted in a wide range.

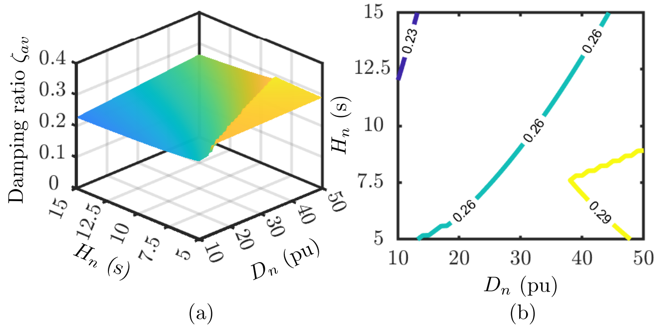

Fig. 40: Damping level assessment in the range of $H_1 \in [5, 15]$ s and $D_1 \in [10, 50]$ pu (a) Damping ratio ζ_{av} (b) Damping ratio contour lines.

4 Development of Self and Mutual Active Damping Strategies

To improve the damping level under the parallel operation of multiple grid-tied VSGs, a novel control scheme as Fig. 41 is developed. Considering the self-induced oscillations caused by the insufficient damping level, the self active damping controller $f_{sn}(s)$ is applied. Moreover, aiming at alleviating the potential interactions among the VSGs, the mutual active damping controller $f_{mn}(s)$ is applied with the help of communications.

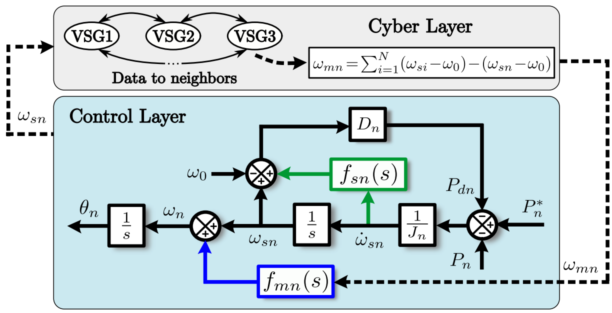

Fig. 41: The proposed self and mutual active damping strategies.

Then, from Fig. 41, the new APC law can be derived as

$$\omega_n = \omega_{sn} + \omega_{mn} f_{mn}(s) \tag{88}$$

$$M_n \dot{\omega}_{sn} = P_n^* - P_n - D_n \left[\omega_{sn} - \omega_0 + f_{sn}(s)\dot{\omega}_{sn}\right] \tag{89}$$

where $\omega_{mn} = \sum_{i=1}^{N}(\omega_{si} - \omega_0) - (\omega_{sn} - \omega_0)$ denotes the sum of VSGs' angular frequency deviation. ω_{sn} denotes the angular frequency from the modified swing equation with the self active damping controller $f_{sn}(s)$.

4.1 Design of the Self Active Damping Controller

Approximately, the external grid is considered as an ideal bus whose voltage amplitude V_0 and frequency ω_g are constant. The VSG is approximately taken as a voltage source whose voltage amplitude is V_0. Then, the nth VSG's output power (without coupling terms) can be formulated as

$$P_n = \frac{3V_0^2}{2X_{en}} \sin \delta_n \approx \frac{3V_0^2}{2X_{en}} \delta_n \tag{90}$$

where $X_{en} = \omega_0 \left(L_g + L_{ln}\right) + X_{vn}$ is the nth VSG's equivalent output impedance.

Assuming that the mutual active damping controller $fmn(s)$ is disabled, ω_n in (88) is equal to ω_{sn}. Substituting (72) and (90) into (89), the closed-loop system $\Delta P_n^* / \Delta P_n$ is

$$f_{pn}(s) = \frac{3V_0^2}{2X_{en}\left[M_n s^2 + D_n f_{sn}(s) s^2 + D_n s\right] + 3V_0^2}. \tag{91}$$

When $f_{sn}(s)$ is disabled, i.e., $f_{sn}(s) = 0$, (91) represents the conventional VSG's APC. Then, from (91), it is clear that the APC loop has two complex eigenvalues, and their natural frequency ω_{on} is

$$\omega_{on} = \sqrt{\frac{3V_0^2}{2X_{en} M_n}}. \tag{92}$$

Moreover, from (91), it can be seen that, when $f_{sn}(s)$ is disabled, the cut-off frequency ω_{cn} of the closed-loop system $\Delta P_n^* / \Delta P_n$ follows

$$20 \log_{10} \left| \frac{3V_0^2}{2X_{en}\left(jD_n \omega_{cn} - M_n \omega_{cn}^2\right) + 3V_0^2} \right| = -3 \text{ dB}. \tag{93}$$

Considering that there is a phase angle difference of $\pi/2$ (at the oscillation frequency ω_{on}) between ω_{sn} and $\dot{\omega}_{sn}$, the self active damping controller $fsn(s)$ is expected to have the same phase angle delay at ω_{on} to enlarge the damping power P_{dn} appropriately during the transient. When it comes to the steady state, i.e., $\dot{\omega}_{sn} = 0$, the damping power P_{dn} is only regulated by the VSG damping constant D_n. To fulfill these requirements, the self active damping controller $fsn(s)$ is selected as

$$f_{sn}(s) = \frac{k_{sn} T_{sn} \omega_{dn}^2}{s^2 + T_{sn} \omega_{dn} s + \omega_{dn}^2} \tag{94}$$

where ω_{dn} is the center frequency of $fsn(s)$ which is set to ω_{on} in (92). k_{sn} and T_{sn} denote two self active damping control coefficients.

When the self active damping regulator $fsn(s)$ is applied, it is expected to improve the damping effect on the oscillations without degrading the APC bandwidth. For this, $fsn(s)$ should help reduce the the magnitude of $f_{pn}(s)$ at the oscillation frequency ω_{on} without affecting the cut-off frequency ω_{cn}. At the same time, the magnitudes of $fsn(s)$ at other frequencies within the bandwidth is expected to be small enough as well. Following these preconditions, the objective can be formulated as

$$\begin{aligned} min \quad & |f_{pn}(j\omega_{on})| \\ s.t. \quad & 20\log_{10}|f_{pn}(j\omega_{cn})| = -3 \text{ dB} \\ & \forall\omega \in [0, \omega_{cn}] \;\; 20\log_{10}|f_{pn}(j\omega)| \leq 3 \text{ dB} \end{aligned} \tag{95}$$

where ω denotes any frequency in the range of $[0, \omega_{cn}]$.

The design of the self active damping control $f_{pn}(s)$ is applied as follows:

Algorithm 1: Design of the self active damping control $f_{pn}(s)$

```
for n ∈ [1, N] do
    Read M_n, D_n and X_en;
    Calculate ω_on according to (92) and let ω_dn = ω_on;
    Solve ω_cn from (93) via fsolve function in Matlab;
    Find k_sn and T_sn from (95) via fmincon function in Matlab;
Output ω_on, k_sn, and T_sn
```

4.2 Design of the Mutual Active Damping Controller

To alleviate the oscillation that is introduced by the interaction among VSGs, the mutual active damping controller $f_{mn}(s)$ is applied as

$$f_{mn}(s) = \frac{k_{mn}\omega_r s}{T_m s^2 + \omega_r s + T_m \omega_r^2} \tag{96}$$

where ω_r is the center frequency where $f_{mn}(s)$ has the maximum gin k_{mn}. T_m denotes the filter selectivity for tuning the pass band. For simplicity, ω_r and T_m can be selected as follows:

$$\omega_r = \sqrt{\omega_l\omega_h},\; T_m = \frac{\sqrt{\omega_l\omega_h}}{\omega_h - \omega_l} \tag{97}$$

where ω_l and ω_h denote the pass band range.

To let the pass band of $f_{mn}(s)$ cover all the oscillation frequencies, we have

$$\forall n \in [1, N] \;\; \omega_l \ll \omega_{on} \ll \omega_h. \tag{98}$$

Here, for simplicity, ω_l and ω_h are set to $0.1\omega_{o,min}$ and $10\omega_{o,max}$, where $\omega_{o,min}$ and $\omega_{o,max}$ denote the oscillation frequency range.

Then, only the coefficient k_{mn} is left to be selected. Substituting (72) and (90) into (88) and (89), $\Delta\omega_{sn}/\Delta\omega_{mn}$ is derived in the sense of small signal as

$$f_{\omega n}(s) = \frac{-3V_0^2 f_{mn}(s)s}{2X_{en}\left(M_n s + D_n f_{sn}(s)s + D_n\right) + 3V_0^2 s}. \tag{99}$$

To let $\Delta\omega_{mn}$ work without affecting the generation of ω_{sn}, $f_{mn}(s)$ should be designed to let $\Delta\omega_{sn}/\Delta\omega_{mn}$ have relatively small magnitudes within the entire frequency range. For example, it can be formulated as

$$\forall\omega \in [0,\infty] \;\; 20\log_{10}|f_{\omega n}(j\omega)| = 15 \text{ dB}. \tag{100}$$

Using (100) and the *getPeakGain* function in MATLAB, the k_{mn} is obtained by iterations. The procedures of designing the mutual active damping controller $f_{mn}(s)$ are shown as follows:

Algorithm 2: Design of the mutual active damping controller $f_{mn}(s)$

Find $\omega_{o,min}$ and $\omega_{o,max}$ among $\omega_{o1}, \omega_{o1}, \ldots, \omega_{oN}$;
Let $\omega_l = 0.1\omega_{o,min}$ and $\omega_h = 10\omega_{o,max}$;
Calculate ω_r and T_m according to (97);
for $n \in [1, N]$ **do**
    while $getPeakGain(f_{\omega n}(s)) < 10^{\frac{-15}{20}}$ **do**
        Increase the value of k_{mn};
Output ω_r, T_m and k_{mn}

5 Simulation and Experimental Validations

5.1 Simulation Validations

Using the system settings and VSG control parameters presented in Table 8 and 9 and applying the control scheme shown in Fig. 41 and design method (i.e., Algorithm 1 and 2), the parameters of the self active damping controller $f_{sn}(s)$ and the mutual active damping controller $f_{mn}(s)$ are obtained and given in Table 10. Subsequently, using these parameters, the system as Fig. 37 is implemented and tested in Digsilent.

Table 10: The parameters of the controllers $f_{sn}(s)$ and $f_{mn}(s)$

VSG	ω_{dn}	k_{sn}	T_{sn}	ω_r	T_m	k_{mn}
1∼3	5.21 rad/s	2.27	3.78	5.21 rad/s	0.21	0.185

When the VSGs are applied without the proposed active damping strategy, VSG angular frequencies ω_n and output power P_n contains sustained oscillations under the power set point changes ($\Delta P_n^* = -0.2$ pu), as depicted in Fig.42(a) and 42(b). When the self-damping controller $f_{sn}(s)$ is applied, most of the oscillations are alleviated, as shown in Fig. 42(c) and 42(d). Only the slight power oscillations caused by the interactions are left. In the case that both $f_{sn}(s)$ and $f_{mn}(s)$ are applied, the output power are decoupled from each other, and the transient is improved without oscillations, as depicted in Fig. 42(e) and 42(f).

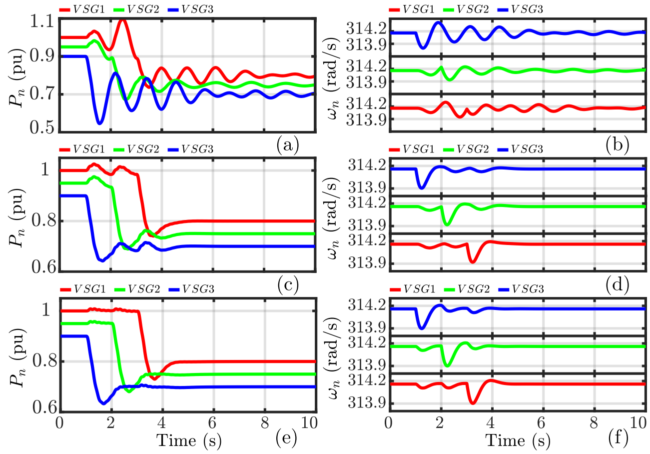

Fig. 42: Responses under the set point changes ($\Delta P_n^* = -0.2$ pu). Conventional VSGs: (a) P_n; (b) ω_n; When $f_{sn}(s)$ is applied: (c) P_n; (d) ω_n; When $f_{sn}(s)$ and $f_{mn}(s)$ are applied: (e) P_n; (f) ω_n.

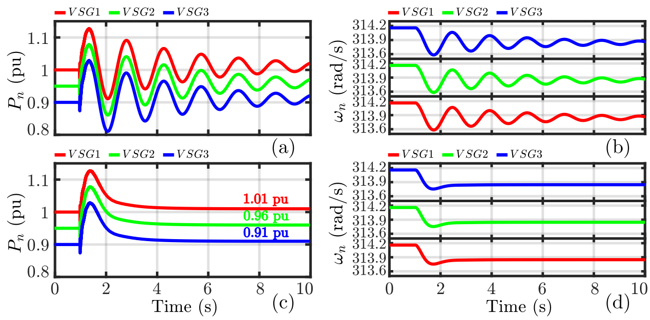

Fig. 43: Responses under the frequency variation ($\Delta f_g = -0.05$ Hz). Conventional VSGs: (a) P_n; (b) ω_n; When the proposed damping algorithm is applied: (c) P_n; (d) ω_n.

As depicted in Fig. 43(a) and 43(b), when a grid frequency step change of -0.05 Hz is applied at 1 second in the simulation, oscillations in both VSG angular frequencies and the output power can be seen. In comparison, once the proposed active damping controllers are applied, these poorly damped oscillations are well attenuated. The inertial response is not degraded by the proposed active damping controllers, and inertial power is generated properly during the transient.

Subsequently, the control scheme and the design are validated under the symmetrical voltage dip (90% of the nominal value). As depicted in Fig. 44(a) and 44(b), after the voltage dip, the proposed active damping strategy works effectively to attenuate the oscillations.

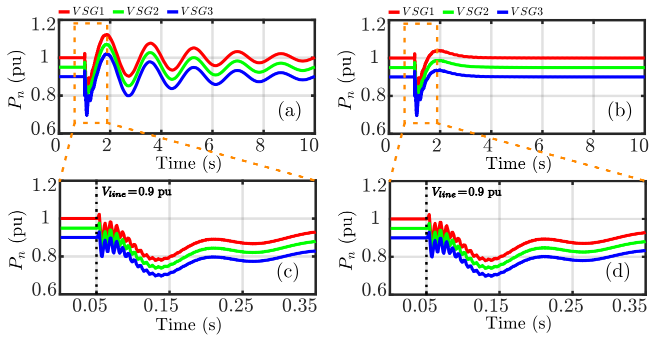

Fig. 44: Responses under the grid voltage dip ($V_{line} = 0.9$ pu). (a) Conventional VSGs output power; (b) Output power of VSGs with the proposed damping strategy; (c) Zoom of the waveform in (a); (d) Zoom of the waveform in (b).

In addition to the poorly damped low frequency oscillations, at the instant of the voltage dip, there are slight power oscillations at a relatively high frequency, as depicted in Fig. 44(c) and 44(d). Since they are not within the control bandwidth, they cannot be effectively attenuated. To suppress these power oscillations, extra active damping strategies need to be included.

5.2 Experimental Validations

In the experimental validations, a scale-down implementation using three 2.2 kVA Danfoss inverters is applied , and it is illustrated by Fig. 45. The external grid is simulated by the Chroma 61845 grid simulator, and the control is realized using the DS1006 processor. The grid-side currents and the VSG output

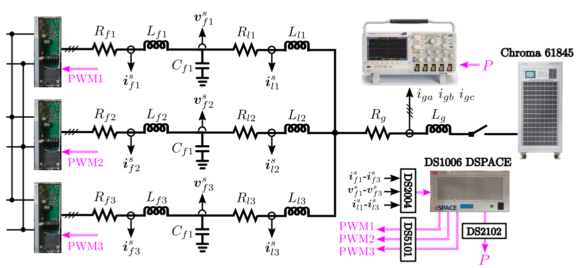

Fig. 45: Experimental setup.

power are measured by the oscilloscope. The settings for the experimental implementation are presented in Table 11.

Table 11: Settings used for the experimental implementation

Variable	Values	Variable	Values	Variable	Values
S_{basen}	2.2 kW	V_{line}	220 V	R_{fn}	0.005 pu
L_{fn}	0.077 pu	C_{fn}	16.08 pu	R_{ln}	0.005 pu
L_{ln}	0.051 pu	R_g	0.018 pu	L_g	0.036 pu
l_{pn}	0.14 pu	l_{in}	9.09 pu	k_{pn}	7.7 pu
k_{in}	1320 pu	R_{vn}	0 pu	X_{vn}	0 pu
T_c	100 μs	H_n	5 s	D_n	10 pu
m_{pn}	0.5 pu	m_{in}	0.25 pu	V_0	180 V
ω_{dn}	19 rad/s	k_{sn}	0.77	T_{sn}	3.89
ω_r	19 rad/s	T_m	0.21	k_{mn}	0.17

As shown in Fig. 46(a), when multiple grid-tied VSGs are applied without the proposed active damping strategy, under an active power set point step change of 0.27 pu, obvious oscillations can be found in the VSG's output. The interactions are obvious as well. In comparison, when multiple grid-tied VSGs are applied with the proposed controllers, the sustained oscillations in Fig. 46(a) are attenuated well, seeing Fig. 46(b). The VSG's power tracking is smooth, and only slight power variations caused by the interactions can be seen in the output.

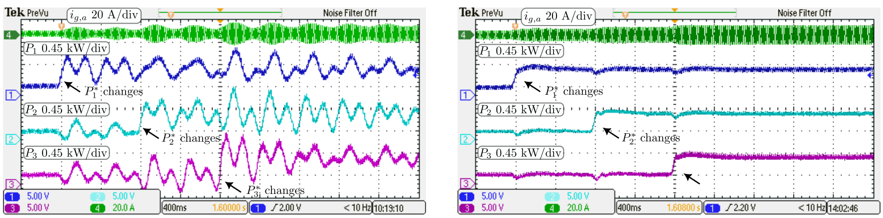

(a) (b)

Fig. 46: Waveform under the set point step change ($\Delta P_n^* = 0.27$ pu). (a) Without the proposed strategy; (b) With the proposed strategy.

Subsequently, a grid frequency step change ($\Delta f_g = -0.1$ Hz) is applied to validate the proposed strategy. As depicted in Fig. 47(a), under the grid frequency perturbation, sustained output power oscillations can be observed when multiple VSGs are applied without any additional damping strategy. In comparison, with the proposed active damping method, these power oscillations are remarkably attenuated, as depicted in Fig. 47(b). From the output power transient in Fig. 47(b), the inertial power is injected in to the grid appropriately, which indicated that the proposed active damping algorithm can preserve the inertial response well.

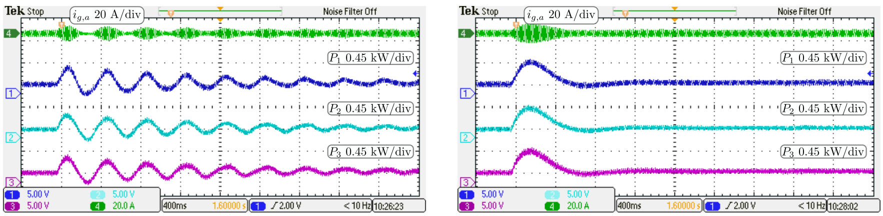

(a) (b)

Fig. 47: Waveform under the frequency step change ($\Delta f_g = -0.1$ Hz). (a) Without the proposed strategy; (b) With the proposed strategy.

As depicted in Fig. 48(a), when a voltage dip ($V_{line} = 0.8$ pu) is applied in the experiment, sustained oscillations appear in the VSG's output. On the other hand, these oscillations are well attenuated by the proposed active damping controllers, as depicted in Fig. 48(b).

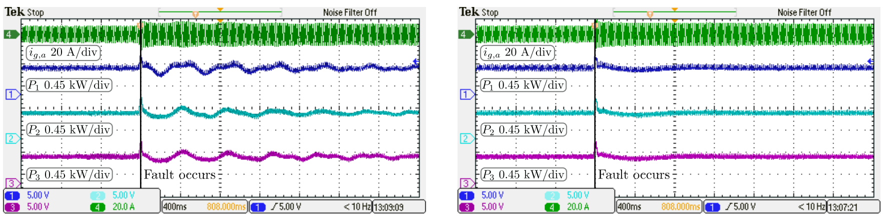

(a) (b)

Fig. 48: Waveform under the voltage dip ($V_{line} = 176$ V). (a) Without the proposed strategy; (b) With the proposed strategy.

6 Summary

In this chapter, a strategy is developed for the parallel operation of multiple grid-tied VSGs. Firstly, the model of multiple grid-tied VSGs is derived using the state-space representation and the Jacobian matrix calculation. Subsequently, based on the derived model, an assessment of the average damping level is conducted. To tackle the lack of damping effects, the self and mutual active damping controllers are developed. Through the simulation and experimental validations under different types of perturbations, the effectiveness of the active damping strategy is validated.

Chapter 6. Conclusions and Future Works

1 Summary

This Ph.D. project focuses on developing active damping strategies for VSG-based AC microgrids. Considering the single VSG operation as well as the parallel operation of multiple VSGs in AC microgrids, active damping strategies using the power control law modification and its optimal tuning were developed in this Ph.D. project. This Ph.D. thesis is summarized as follows:

In *Chapter 1*, the status of the renewable energy system and its integration approaches have been discussed. For the renewables that cannot be arranged in large-scale power plants, the AC microgrid provides a feasible grid integration solution. As a power-electronic-based energy system, the AC microgrid itself often lacks phythical inertia to slow down the frequency dynamic. When it is connected to the grid with a low inertia level, it may not be able to maintain the system stability as expected. This motivates the replacement of conventional GFL control with the GFM control as the GFM inverters operate like controllable voltage sources which share strong similarities with the synchronous machine.

As there are various GFM control methods have been developed, in *Chapter 2*, a review of the typical GFM controls has been conducted. Specifically, it covers the droop control, VSG, PSC, VOC, and matching control. Compared with other GFM controls, the VSG not only provides a good compatibility with the mature vector current-voltage control but also enables a straightforward inertia emulation. On the other hand, its inertia emulation based on the conventional swing equation also leads to restricted stability boundaries and inefficient damping effects, which in turn may cause poorly damped power oscillations.

To alleviate the power oscillations, various active damping control strategies have been proposed. Nevertheless, because VSG's inertia effect is often disregarded during the controller development, the resulting active damping controllers may degrade the inertial response significantly. Considering this drawback, in *Chapter 3*, a power reference feedforward control scheme is firstly proposed. Different from the existing works, the proposed control scheme enables a quantitative design of the power set point tracking without affecting VSG's original inertial response. Considering that a preservation of VSG's inertial response may not be enough for the inertia support in the future power system, it is better to attain a remarkable enhancement in VSG's inertial response and a well-damped power control simultaneously. For this, an combination of the FOC and the VSG is investigated. With extended degrees of freedom included, the proposed FOVSG control scheme provides an inertial response enhancement and a well-damping control.

In *Chapter 4*, considering the accuracy of the small-signal modeling adopting the phaosr representation will be degraded in the case of a limited current-voltage control bandwidth and a large control latency, an improved small-signal model based on the state space representation is firstly derived. Using the eigenvalue analysis, the VSG control parameters are divided into two sets, where one is for the stability adjustment, and another is for the power control dynamic adjustment. Then, a two-step optimization is proposed for the optimal VSG tuning, where the first-step optimization is applied for the extended stability margin, and the second-step optimization is applied for smoothing the power control transient.

In *Chapter 5*, the active-damping strategy development is extended from a single unit operation to the parallel operation of multiple grid-tied VSGs. For this, a small-signal model is derived using the state space representation and the Jacobian matrix calculation. Through the damping level assessment, it is found that the system can be poorly damped in a wide range of inertia and damping constants. To improve the system damping effect on attenuating self-induced and mutually induced power oscillations, self and mutual active damping controllers have been proposed. For the benefit of real-time implementation, a control parameter tuning algorithm that enables the online realization has been developed as well.

2 Main Contributions

The main contributions made in this Ph.D. project are as follows:

- **Feedforward VSG control scheme**

  A novel VSG control scheme using the power set point feedforward has been proposed. Adopting this VSG control scheme, the poorly damped power oscillations in the power set point tacking transient can be significantly alleviated to have a desired dynamic response. Furthermore, the inertial response is preserved well without any degradation.

- **Fractional order VSG control scheme**

  A novel VSG control scheme using the fractional order regulator is proposed. Applying this control scheme, extended degrees of freedom can be involved in the control performance adjustment, which introduces a remarkable improvement of the power control damping level and the inertial response, simultaneously.

- **Stability-oriented VSG optimal tuning algorithm**

  A stability-oriented VSG tuning algorithm has been proposed. The proposed tuning algorithm enables an optimization of the VSG control stability and the power control dynamic, which benefits maintaining the control performance under different operation conditions.

- **An active damping control strategy for the parallel operation of multiple grid-tied VSGs**

  Considering the parallel operation of multiple grid-tied VSGs, an active damping control strategy which includes both self and mutual active damping controllers have been proposed. Applying the proposed control strategy and tuning algorithm, the output power of VSGs are well-damped and decoupled from each other, and the preferable inertial response can be preserved well.

3 Future Research Perspectives

The future research perspectives are summarized as follows:

- The VSG modeling and analysis applied in this Ph.D. project have been conducted in the sense of small signal; however, in practice, perturbations like short-circuit faults are more critical. Therefore, the transient stability, the resulting wide-band oscillations, the prevention of overloading need to be further investigated.
- The DC-link is considered as ideal in this Ph.D. project, which means its energy storage is considered as infinite. Nevertheless, in practice, the energy storage are often restricted, and the DC-link dynamic will be inevitably affected by the inverter controllers. In this sense, the VSG control needs to be further investigated with DC-link dynamics involved.
- In this Ph.D. project, the operation of multiple VSGs in an AC microgrid has been investigated , where the grid interconnection is simplified as a impedance. However, in practice, the topology of the grid network and the interconnections are much complex. In this sense, the modeling and control of VSGs inside complex networks are of research significance.

Bibliography

References

[1] IEA. (2022) World energy outlook 2022. [Online]. Available: https://www.iea.org/reports/world-energy-outlook-2022

[2] M. Liserre, T. Sauter, and J. Y. Hung, "Future energy systems: Integrating renewable energy sources into the smart power grid through industrial electronics," *IEEE Industrial Electronics Magazine*, vol. 4, no. 1, pp. 18–37, Mar. 2010.

[3] IEA. (2022) Wind electricity. [Online]. Available: https://www.iea.org/reports/wind-electricity

[4] IEA. (2022) Solar pv. [Online]. Available: https://www.iea.org/reports/solar-pv

[5] IEA. (2021) Net zero by 2050. [Online]. Available: https://www.iea.org/reports/net-zero-by-2050

[6] Y. Lin *et al.*, "Research roadmap on grid-forming inverters," National Renewable Energy Lab.(NREL), Golden, CO (United States), Tech. Rep., 2020.

[7] Ørsted. (2022) Hornsea 1 wind farm. [Online]. Available: https://orsted.co.uk/energy-solutions/offshore-wind/our-wind-farms

[8] J. M. Guerrero, J. C. Vasquez, J. Matas, L. G. de Vicuna, and M. Castilla, "Hierarchical control of droop-controlled AC and DC microgrids—a general approach toward standardization," *IEEE Transactions on Industrial Electronics*, vol. 58, no. 1, pp. 158–172, Jan. 2011.

[9] A. Hirsch, Y. Parag, and J. M. Guerrero, "Microgrids: A review of technologies, key drivers, and outstanding issues," *Renewable and Sustainable Energy Reviews*, vol. 90, pp. 402–411, Jul. 2018.

[10] Siemens. (2022) Siemens campus microgrid. [Online]. Available: https://new.siemens.com/at/en/company/topic-areas/siemens-campus-microgrid.html

[11] K. S. Rajesh, S. S. Dash, R. Rajagopal, and R. Sridhar, "A review on control of ac microgrid," *Renewable and Sustainable Energy Reviews*, vol. 71, pp. 1364–0321, May. 2017.

[12] J. M. Guerrero, M. Chandorkar, T. L. Lee, and P. C. Loh, "Advanced control architectures for intelligent microgrids—part I: Decentralized and hierarchical control," *IEEE Transactions on Industrial Electronics*, vol. 60, no. 4, pp. 1254–1262, Apr. 2013.

[13] J. Rocabert, A. Luna, F. Blaabjerg, and P. Rodríguez, "Ieee transactions on power electronics," *Control of Power Converters in AC Microgrids*, vol. 27, no. 11, pp. 4734–4749, Nov. 2012.

[14] ENTSO-E Technical Group on High Penetration of Power Electronic Interfaced Power Sources. (2020) High penetration of power electronic interfaced power sources and the potential contribution of grid forming converters. [Online]. Available: https://windeurope.org/intelligence-platform/product/high-penetration-of-power-electronic-interfaced-power-sources/

[15] P. Kundur *et al.*, "Definition and classification of power system stability," *IEEE Transactions on Power Systems*, vol. 19, no. 3, pp. 1387–1401, Aug. 2004.

[16] N. Hatziargyriou *et al.*, "Definition and classification of power system stability – revisited and extended," *IEEE Transactions on Power Systems*, vol. 36, no. 4, pp. 3271–3281, Jul. 2021.

[17] H. Geng, L. Liu, and R. Li, "Synchronization and reactive current support of pmsg-based wind farm during severe grid fault," *IEEE Transactions on Sustainable Energy*, vol. 9, no. 4, pp. 1596–1604, Oct. 2018.

[18] S. Ma, H. Geng, L. Liu, G. Yang, and B. C. Pal, "Grid-synchronization stability improvement of large scale wind farm during severe grid fault," *IEEE Transactions on Power Systems*, vol. 33, no. 1, pp. 216–226, Jan. 2018.

[19] N. Bottrell and T. C. Green, "Comparison of current-limiting strategies during fault ride-through of inverters to prevent latch-up and wind-up," *IEEE Transactions on Power Electronics*, vol. 29, no. 7, pp. 3786–3797, Jul. 2014.

[20] O. Kahouli, M. Jebali, B. Alshammari, and H. H. Abdallah, "PSS design for damping low-frequency oscillations in a multi-machine power system with penetration of renewable power generations," *IET Renewable Power Generation*, vol. 13, no. 1, pp. 116–127, Jan. 2019.

[21] C. Liu and G. Cai, "Power-oscillation evaluation in power systems with high penetration of renewable power generation based on network virtual inertia," *IET Renewable Power Generation*, vol. 13, no. 1, pp. 138–145, Jan. 2019.

[22] N. R. Ullah, K. Bhattacharya, and T. Thiringer, "Wind farms as reactive power ancillary service providers—technical and economic issues," *IEEE Transactions on Energy Conversion*, vol. 24, no. 3, pp. 661–672, Sept. 2009.

[23] J. C. Vasquez, R. A. Mastromauro, J. M. Guerrero, and M. Liserre, "Voltage support provided by a droop-controlled multifunctional inverter," *IEEE Transactions on Industrial Electronics*, vol. 56, no. 11, pp. 4510–4519, Nov. 2009.

[24] J. Morren, S. W. H. de Haan, W. L. Kling, and J. A. Ferreira, "Wind turbines emulating inertia and supporting primary frequency control," *IEEE Transactions on Power Systems*, vol. 21, no. 1, pp. 433–434, Feb. 2006.

[25] J. Alipoor, Y. Miura, and T. Ise, "Power system stabilization using virtual synchronous generator with alternating moment of inertia," *IEEE Journal of Emerging and Selected Topics in Power Electronics*, vol. 3, no. 2, pp. 451–458, Jun. 2015.

[26] National Grid ESO. (2021) Technical report on the events of 9 august 2019. [Online]. Available: https://www.nationalgrideso.com/document/152346/download

[27] J. L. Agorreta, M. Borrega, J. López, and L. Marroyo, "Modeling and control of N-paralleled grid-connected inverters with LCL filter coupled due to grid impedance in PV plants," *IEEE Transactions on Power Electronics*, vol. 26, no. 3, pp. 770–785, Mar. 2011.

[28] X. Wang, Y. He, D. Pan, H. Zhang, Y. Ma, and X. Ruan, "Harmonic instability of LCL-type grid-connected inverter caused by the pole-zero cancellation: A case study," *IEEE Transactions on Industrial Electronics*, vol. 69, no. 11, pp. 11 580–11 589, Nov. 2022.

[29] S. Zhang, S. Jiang, X. Lu, B. Ge, and F. Z. Peng, "Resonance issues and damping techniques for grid-connected inverters with long transmission cable," *IEEE Transactions on Power Electronics*, vol. 29, no. 1, pp. 110–120, Jan. 2014.

[30] L. Wang, X. Xie, Q. Jiang, H. Liu, Y. Li, and H. Liu, "Investigation of SSR in practical DFIG-based wind farms connected to a series-compensated power system," *IEEE Transactions on Power Systems*, vol. 30, no. 5, pp. 2772–2779, Sept. 2015.

[31] H. A. Mohammadpour and E. Santi, "Modeling and control of gate-controlled series capacitor interfaced with a DFIG-based wind farm," *IEEE Transactions on Industrial Electronics*, vol. 62, no. 2, pp. 1022–1033, Feb. 2015.

[32] D. B. Rathnayake *et al.*, "Grid forming inverter modeling, control, and applications," *IEEE Access*, vol. 9, pp. 114 781–114 807, Aug. 2021.

[33] J. Matevosyan *et al.*, "Grid-forming inverters: Are they the key for high renewable penetration?" *IEEE Power and Energy Magazine*, vol. 17, no. 6, pp. 89–98, Nov.-Dec. 2019.

[34] H. Bevrani, T. Ise, and Y. Miura, "Virtual synchronous generators: A survey and new perspectives," *International Journal of Electrical Power & Energy Systems*, vol. 54, pp. 244–254, Jan. 2014.

[35] T. Shintai, Y. Miura, and T. Ise, "Oscillation damping of a distributed generator using a virtual synchronous generator," *IEEE Transactions on Power Delivery*, vol. 29, no. 2, pp. 668–676, Apr. 2014.

[36] J. Liu, Y. Miura, and T. Ise, "Fixed-parameter damping methods of virtual synchronous generator control using state feedback," *IEEE Access*, vol. 7, pp. 99 177–99 190, 2019.

[37] J. Liu, Y. Miura, and T. Ise, "A comparative study on damping methods of virtual synchronous generator control," in *2019 21st European Conference on Power Electronics and Applications (EPE '19 ECCE Europe)*, 2019, pp. 1–10.

[38] Z. Qu, J. C. H. Peng, H. Yang, and D. Srinivasan, "Modeling and analysis of inner controls effects on damping and synchronizing torque components in VSG-controlled converter," *IEEE Transactions on Energy Conversion*, vol. 36, no. 1, pp. 488–499, Mar. 2021.

[39] J. Driesen and K. Visscher, "Virtual synchronous generators," in *2008 IEEE Power and Energy Society General Meeting - Conversion and Delivery of Electrical Energy in the 21st Century*, Pittsburgh, PA, USA, Jul. 2008, pp. 1–3.

[40] Q. Zhong and G. Weiss, "Static synchronous generators for distributed generation and renewable energy," in *2009 IEEE/PES Power Systems Conference and Exposition*, Seattle, WA, USA, Mar. 2009, pp. 1–6.

[41] M. Chen, D. Zhou, and F. Blaabjerg, "Modelling, implementation, and assessment of virtual synchronous generator in power systems," *Journal of Modern Power Systems and Clean Energy*, vol. 8, no. 3, pp. 399–411, May. 2020.

[42] H.-P. Beck and R. Hesse, "Virtual synchronous machine," in *2007 9th International Conference on Electrical Power Quality and Utilisation*, Barcelona, Spain, Oct. 2007, pp. 1–6.

[43] Y. Chen, R. Hesse, D. Turschner, and H.-P. Beck, "Comparison of methods for implementing virtual synchronous machine on inverters," in *International Conference on Renewable Energies and Power Quality*, Santiago de Compostela, Spain, Mar. 2012, pp. 734–739.

[44] S. D'Arco, J. A. Suul, and O. B. Fosso, "Automatic tuning of cascaded controllers for power converters using eigenvalue parametric sensitivities," *IEEE Transactions on Industry Application*, vol. 51, no. 2, pp. 1743–1753, Mar. 2015.

[45] L. Huang, H. Xin, and Z. Wang, "Damping low-frequency oscillations through VSC-HVDC stations operated as virtual synchronous machines," *IEEE Transactions on Power Electronics*, vol. 34, no. 6, p. 5803–5818, Jun. 2019.

[46] Q. Zhong and G. Weiss, "Synchronverters: Inverters that mimic synchronous generators," *IEEE Transactions on Industrial Electronics*, vol. 58, no. 4, pp. 1259–1267, Apr. 2011.

[47] Q. Zhong, P. Nguyen, Z. Ma, and W. Sheng, "Self-synchronized synchronverters: Inverters without a dedicated synchronization unit," *IEEE Transactions on Power Electronics*, vol. 29, no. 2, pp. 617–630, Feb. 2014.

[48] L. Zhang, L. Harnefors, and H. Nee, "Power-synchronization control of grid-connected voltage-source converters," *IEEE Transactions on Power Systems*, vol. 25, no. 2, pp. 809–820, May. 2010.

[49] L. Zhang, L. Harnefors, and H. Nee, "Interconnection of two very weak AC systems by VSC-HVDC links using power-synchronization control," *IEEE Transactions on Power Systems*, vol. 26, no. 1, pp. 344–355, Feb. 2011.

[50] J. Z. Zhou, H. Ding, S. Fan, Y. Zhang, and A. M. Gole, "Impact of short-circuit ratio and phase-locked-loop parameters on the small-signal behavior of a VSC-HVDC converter," *IEEE Transactions on Power Delivery*, vol. 29, no. 5, pp. 2287–2296, Oct. 2014.

[51] S. V. Dhople, B. B. Johnson, and A. O. Hamadeh, "Virtual oscillator control for voltage source inverters," in *2013 51st Annual Allerton Conference on Communication, Control, and Computing (Allerton)*, Monticello, IL, USA, 2013, pp. 1359–1363.

[52] S. V. Dhople, B. B. Johnson, F. Dörfler, and A. O. Hamadeh, "Synchronization of nonlinear circuits in dynamic electrical networks with general topologies," *IEEE Transactions on Circuits and Systems I: Regular Papers*, vol. 61, no. 9, pp. 2677–2690, Sept. 2014.

[53] B. B. Johnson, S. V. Dhople, A. O. Hamadeh, and P. T. Krein, "Synchronization of parallel single-phase inverters with virtual oscillator control," *IEEE Transactions on Power Electronics*, vol. 29, no. 11, pp. 6124–6138, Nov. 2014.

[54] B. B. Johnson, S. V. Dhople, J. L. Cale, A. O. Hamadeh, and P. T. Krein, "Oscillator-based inverter control for islanded three-phase microgrids," *IEEE Journal of Photovoltaics*, vol. 4, no. 1, pp. 387–395, Jan. 2014.

[55] M. Sinha, F. Dörfler, B. B. Johnson, and S. V. Dhople, "Uncovering droop control laws embedded within the nonlinear dynamics of van der pol oscillators," *IEEE Transactions on Control of Network Systems*, vol. 4, no. 2, pp. 347–358, Jun. 2017.

[56] D. Raisz, T. T. Thai, and A. Monti, "Power control of virtual oscillator controlled inverters in grid-connected mode," *IEEE Transactions on Power Electronics.*, vol. 34, no. 6, pp. 5916–5926, Jun. 2019.

[57] M. A. Awal, H. Yu, H. Tu, S. M. Lukic, and I. Husain, "Hierarchical control for virtual oscillator based grid-connected and islanded microgrids," *IEEE Transactions on Power Electronics*, vol. 35, no. 1, pp. 988–1001, Jan. 2020.

[58] D. Groß, M. Colombino, J. Brouillon, and F. Dörfler, "The effect of transmission-line dynamics on grid-forming dispatchable virtual oscillator control," *IEEE Transactions on Control of Network Systems*, vol. 6, no. 3, pp. 1148–1160, Sept. 2019.

[59] M. Colombino, D. Groß, J. Brouillon, and F. Dörfler, "Global phase and magnitude synchronization of coupled oscillators with application to the control of grid-forming power inverters," *IEEE Transactions on Automatic Control*, vol. 64, no. 11, pp. 4496–4511, Nov. 2019.

[60] C. Arghir, T. Jouini, and F. Dörfler, "Grid-forming control for power converters based on matching of synchronous machines," *Automatica*, vol. 95, pp. 273–282, Sept. 2018.

[61] C. Arghir and F. Dörfler, "The electronic realization of synchronous machines: Model matching, angle tracking, and energy shaping techniques," *IEEE Transactions on Power Electronics*, vol. 35, no. 4, pp. 4398–4410, Apr. 2020.

[62] J. Liu, Y. Miura, and T. Ise, "Comparison of dynamic characteristics between virtual synchronous generator and droop control in inverter-based distributed generators," *IEEE Transactions on Power Electronics*, vol. 31, no. 5, pp. 3600–3611, 2016.

[63] J. Fang, Y. Tang, H. Li, and X. Li, "A battery/ultracapacitor hybrid energy storage system for implementing the power management of virtual synchronous generators," *IEEE Transactions on Power Electronics*, vol. 38, no. 4, pp. 2820–2824, 2018.

[64] X. Meng, J. Liu, and Z. Liu, "A generalized droop control for grid-supporting inverter based on comparison between traditional droop control and virtual synchronous generator control," *IEEE Transactions on Power Electronics*, vol. 34, no. 6, pp. 5416–5438, 2019.

[65] W. Du, Q. Fu, and H. F. Wang, "Power system small-signal angular stability affected by virtual synchronous generators," *IEEE Transactions on Power Systems*, vol. 34, no. 4, p. 3209–3219, 2019.

[66] S. Dong and Y. C. Chen, "Adjusting synchronverter dynamic response speed via damping correction loop," *IEEE Transactions on Power Electronics*, vol. 32, no. 2, pp. 608–619, Jun. 2017.

[67] Z. Shuai, W. Huang, Z. J. Shen, A. Luo, and Z. Tian, "Active power oscillation and suppression techniques between two parallel synchronverters during load fluctuations," *IEEE Transactions on Power Electronics*, vol. 35, no. 4, pp. 4127–4142, Apr. 2020.

[68] M. Chen, D. Zhou, and F. Blaabjerg, "Active power oscillation damping based on acceleration control in paralleled virtual synchronous generators system," *IEEE Transactions on Power Electronics*, vol. 36, no. 8, pp. 9501–9510, Aug. 2021.

[69] S. Golestan, J. M. Guerrero, and J. C. Vasquez, "Three-phase PLLs: A review of recent advances," *IEEE Transactions on Power Electronics*, vol. 32, no. 3, pp. 1894–1907, 2017.

[70] Y. Yu *et al.*, "A comparison of fixed-parameter active-power-oscillation damping solutions for virtual synchronous generators," in *IECON 2021 – 47th Annual Conference of the IEEE Industrial Electronics Society*, Toronto, ON, Canada, 2021, pp. 1–6.

[71] H. Wu *et al.*, "Small-signal modeling and parameters design for virtual synchronous generators," *IEEE Transactions on Industrial Electronics*, vol. 63, no. 7, pp. 4292–4303, 2016.

[72] J. He and Y. W. Li, "Analysis, design, and implementation of virtual impedance for power electronics interfaced distributed generation," *IEEE Transactions on Industry Applications*, vol. 47, no. 6, pp. 2525–2538, 2011.

[73] R. W. Erickson and D. Maksimovic, *Fundamentals of Power Electronics*, 2nd ed. Norwell, MA, USA: Kluwer, 2001.

[74] Y. Yu *et al.*, "A reference-feed-forward-based damping method for virtual synchronous generator control," *IEEE Trans. Power Electron.*, vol. 37, no. 7, pp. 7566–7571, Jul. 2022.

[75] C. A. Monje, Y. Chen, B. M. Vinagre, D. Xue, and V. Feliu-Batlle, *Fractional-order Systems and Controls*, 1st ed. London, U.K.: Springer-Verlag, 2010.

[76] D. B. Rathnayake, R. Razzaghi, and B. Bahrani, "Generalized virtual synchronous generator control design for renewable power systems," *IEEE Transactions on Sustainable Energy*, vol. 13, no. 2, pp. 1021–1036, Apr. 2022.

[77] A. Oustaloup, F. Levron, B. Mathieu, and F. M. Nanot, "Frequency-band complex noninteger differentiator: characterization and synthesis," *IEEE Transactions on Circuits and Systems I: Regular Papers*, vol. 47, no. 1, pp. 25–39, Jan. 2000.

[78] G. F. Franklin, J. D. Powell, and A. Emami-Naeini, *Feedback control of dynamic systems*, 8th ed. Prentice hall Upper Saddle River, 2002.

[79] H. Wu and X. Wang, "A mode-adaptive power-angle control method for transient stability enhancement of virtual synchronous generators," *IEEE Journal of Emerging and Selected Topics in Power Electronics*, vol. 8, no. 2, pp. 1034–1049, Jun. 2020.

[80] X. Xiong, C. Wu, B. Hu, D. Pan, and F. Blaabjerg, "Transient damping method for improving the synchronization stability of virtual synchronous generators," *IEEE Journal of Emerging and Selected Topics in Power Electronics*, vol. 36, no. 7, pp. 7820–7831, Jul. 2021.

[81] J. Chen and T. O'Donnell, "Parameter constraints for virtual synchronous generator considering stability," *IEEE Transactions on Power Systems*, vol. 34, no. 3, pp. 2479–2481, May. 2019.

[82] T. Qoria, F. Gruson, F. Colas, X. Guillaud, M.-S. Debry, and T. Prevost, "Tuning of cascaded controllers for robust grid-forming voltage source converter," in *2018 Power Systems Computation Conference (PSCC)*, 2018, pp. 1–7.

[83] S. Dong and Y. C. Chen, "Dynamic modelling requirements for tuning of cascaded voltage and current loops in VSMs," in *IECON 2021 – 47th Annual Conference of the IEEE Industrial Electronics Society*, 2021, pp. 1–6.

[84] K. Shi, Y. Wang, Y. Sun, P. Xu, and F. Gao, "Frequency-coupled impedance modeling of virtual synchronous generators," *IEEE Transactions on Power Systems*, vol. 36, no. 4, pp. 3692–3700, Jul. 2021.

[85] Y. Xu, H. Nian, B. Hu, and D. Sun, "Impedance modeling and stability analysis of VSG controlled type-IV wind turbine system," *IEEE Transactions on Energy Conversion*, vol. 36, no. 4, pp. 3438–3448, Dec. 2021.

[86] M. R. AlRashidi and M. E. El-Hawary, "A survey of particle swarm optimization applications in electric power systems," *IEEE Transactions on Evolutionary Computation*, vol. 13, no. 4, pp. 913–918, Aug. 2009.

[87] W. Tang, J. Hu, Y. Chang, and F. Liu, "Modeling of DFIG-based wind turbine for power system transient response analysis in rotor speed control timescale," *IEEE Transactions on Power Systems*, vol. 33, no. 6, p. 6795–6805, Nov. 2018.

[88] J. Kennedy and R. Eberhart, "Particle swarm optimization," in *Proceedings of IEEE International Conference on Neural Networks*, vol. 4, Perth, Australia, 1995, p. 1942–1948.

[89] R. C. Dorf and R. H. Bishop, *Modern Control Systems*, 12th ed. Englewood Cliffs, NJ, USA:Pearson, 2011.

[90] C. Canizares *et al.*, "Benchmark models for the analysis and control of small-signal oscillatory dynamics in power systems," *IEEE Transactions on Power Systems*, vol. 32, no. 1, pp. 715–722, Jan. 2017.

[91] Y. Yang *et al.*, "A new virtual inductance control method for frequency stabilization of grid forming virtual synchronous generators," *IEEE Trans. Ind. Electron.*, vol. 70, no. 1, pp. 441–451, Jan. 2022.

[92] F. Wang, L. Zhang, X. Feng, and H. Guo, "An adaptive control strategy for virtual synchronous generator," *IEEE Trans. Ind. Appl.*, vol. 54, no. 5, pp. 5124–5133, Sept. 2018.

[93] Z. Wang, Y. Yu, W. Gao, M. Davari, and C. Deng, "Adaptive, optimal, virtual synchronous generator control of three-phase grid-connected inverters under different grid conditions—an adaptive dynamic programming approach," *IEEE Trans. Ind. Inform.*, vol. 18, no. 11, pp. 7388–7399, Nov. 2022.

[94] D. Li, Q. Zhu, S. Lin, and X. Y. Bian, "A self-adaptive inertia and damping combination control of VSG to support frequency stability," *IEEE Trans. Energy Convers.*, vol. 32, no. 1, pp. 397–398, Mar. 2017.

[95] J. Alipoor, Y. Miura, and T. Ise, "Stability assessment and optimization methods for microgrid with multiple VSG units," *IEEE Trans. Smart Grid*, vol. 9, no. 2, pp. 1462–1471, Mar. 2018.

[96] M. Chen, D. Zhou, C. Wu, and F. Blaabjerg, "Characteristics of parallel inverters applying virtual synchronous generator control," *IEEE Trans. Smart Grid*, vol. 12, no. 6, pp. 4690–4701, Nov. 2021.

[97] S. Fu *et al.*, "Power oscillation suppression of multi-VSG grid via decentralized mutual damping control," *IEEE Trans. Ind. Electron.*, vol. 69, no. 10, pp. 10 202–10 214, Oct. 2022.

[98] P. Sun, J. Yao, Y. Zhao, X. Fang, and J. Cao, "Stability assessment and damping optimization control of multiple grid-connected virtual synchronous generators," *IEEE Trans. Energy Convers.*, vol. 36, no. 4, pp. 3555–3567, Dec. 2021.

Part II

Selected Publications

Paper A

A Reference-Feedforward-Based Damping Method for Virtual Synchronous Generator Control

Yun Yu et al.

The paper has been published in the
IEEE Transactions on Power Electronics Vol. 37(7), pp. 7566-7571, 2022.

Paper B

Fractional Order Virtual Synchronous Generator

Yun Yu et al.

The paper has been accepted by the
IEEE Transactions on Power Electronics

The layout has been revised.

Paper C

Multi-Objective Optimal Tuning of Virtual Synchronous Generators With Feedforward Filters

Yun Yu et al.

The paper has been submitted to the
Applied Energy

Paper D

Active Damping for Dynamic Improvement of Multiple Grid-Tied Virtual Synchronous Generators

Yun Yu et al.

The paper has been submitted to the
IEEE Transactions on Industrial Electronics

Paper E

An Overview of Grid-Forming Control for Wind Turbine Converters

Yun Yu et al.

The paper has been published in the
47th Annual Conference of the IEEE Industrial Electronics Society, 2021, pp. 1-6

Paper F

A Comparison of Fixed-Parameter Active-Power-Oscillation Damping Solutions for Virtual Synchronous Generators

Yun Yu et al.

The paper has been published in the
47th Annual Conference of the IEEE Industrial Electronics Society, 2021, pp. 1-6

The layout has been revised.

Paper G

Accuracy Assessment of Reduced- and Full-Order Virtual Synchronous Generator Models Under Different Grid Strength Cases

Yun Yu et al.

The paper has been published in the
48th Annual Conference of the IEEE Industrial Electronics Society, 2022, pp. 1-6

ISSN (online): 2446-1636
ISBN (online): 978-87-7573-756-7

AALBORG UNIVERSITY PRESS